UNIVERSITAT POLITÈCNICA
DE CATALUNYA

Model order reduction in variational multi-scale problem

Caroline Ferdinand

June 2011

Master Erasmus Mundus in Computational Mechanics

Supervisors: Professor Javier Oliver
Doctor Alfredo E. Huespe

Abstract

The resolution of solid mechanics problems implying complex multi-phase materials or composites materials requires paying special attention to the micro-structure of these materials. The homogenisation procedure, in the context of the Finite Element numerical approaches, enables to treat such multi-scale problems by solving, for each Gauss point of the macroscopic mesh, a micro-scale problem to determine the local constitutive equation. The purpose of this Master thesis is to apply model order reduction techniques to the micro-scale problem. As a single reduction of the displacement space is not efficient enough, a hyper-reduction method is proposed to solve the micro-scale problem. This method, based on the Gappy Data Reconstruction technique, makes it possible to entirely reconstruct the stress tensor using the computational results of a couple of stress components and a stress basis. By reducing the resolution to a given set of stress components and working in a reduced displacement space the computational cost of the micro-scale problem considerably decreases without losing accuracy.

Acknowledgments

I would like to express my gratitude to my supervisors Professor Javier Oliver from the Department of Strength of Materials and Structural Analysis of the Universitat Politècnica de Catalunya and Doctor Alfredo E. Huespe from CIMEC/CONICET of the Universidad Nacional del Litoral, Argentina, for giving me guidance, support and information. They have always been available to help me whatever the distance. I also want to thank the PhD Student Manuel Alejandro Caicedo with who I have worked during this thesis. I have appreciated this collaboration and wish him all the best in the continuation of his PhD thesis on this captivating subject.

Contents

Chapter 1:

Introduction

1.1 Motivation

To provide a constitutive modelling of materials with complex micro-structure, such as composite materials, it is necessary to adopt a multi-scale approach dealing with different length scales, two in the present proposal: the macroscopic scale for the phenomenological behaviour of the solid and the microscopic scale to describe the small scale structure of the material.

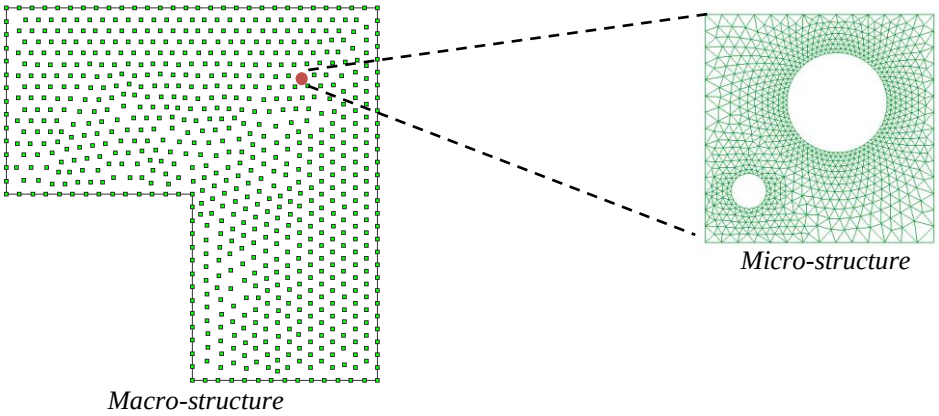

Figure 1.1: Multi-scale problem diagram

The homogenisation technique makes it possible to deal more easily with these two scales. The idea of this technique is to determine a constitutive equation for each Gauss point of the macroscopic mesh, which implies solving a complete sub-problem for each Gauss point. The computational cost of the resolution of such multi-scale problem becomes huge as the problem requires a fine mesh.

The purpose of this thesis is to decrease the size of the system involved in the resolution of the problem at the micro-scale, by applying projection-based Model Order Reduction techniques. But, as shown later, it actually needs to go further than a first step of reduction and apply a hyper-reduction of the micro-scale problem to achieve an interesting speed up in comparison to the classical finite element multi-scale model.

1.2 Background

Over the last years, in order to provide more accurate models for the analysis of the complex materials with microstructure, the interest for the multi-scale approach has increased.

E.A. de Souza Neto and R.A. Feijóo have studied the homogenisation theory of solids based on the volume averaging of the microscopic strain and stress fields over a representative volume element (RVE), see [6].The Hill-Mandel Principle of Macro-Homogeneity, in this approach, is a milestone in order to develop a correct averaging procedure. These authors have established a complete kinematical variational formulation of multi-scale solid constitutive models.

The Model Order Reduction is based on the Proper Orthogonal Decomposition which has been largely studied in the past. The papers of Y.C. Liang, H.P. Lee, S.P. Lim, W.Z. Lin, K.H. Lee & C.G. Wu [9] and S. Volkwein [11] developed the mathematical theory of this technique.

K. Carlberg & C. Farhat [2] [3] [4] and D. Ryckelynck [10] have worked on the application, in finite elements models, of model order reduction techniques and realized the necessity to go further than the simple reduction of the displacement space to

achieve efficient speed up. The first ones proposed to construct POD-reduced bases for the residue of the internal forces and the Jacobian, and apply Gappy Data Reconstruction to reduce the computational cost. The second one proposed to use the hyper-reduction to compute the internal variables.

The Gappy Data Reconstruction has originally been used for image reconstruction by Everson R. & Sirovich L. in the reference [7], a posterior application for estimating missing points in the resolution of computational fluid dynamics problems was presented by P. Astrid, S. Weiland, K. Willcox, & T. Backx [1].

The hyper-reduction performed in this thesis also uses the Gappy Data Reconstruction but to evaluate the stress tensor after determining a POD-reduced stress basis.

1.3 Objectives

The starting material of the thesis is a Matlab finite element code developed by P.J. Sánchez and S.Toro.

Three objectives are pursued in this work:

i) The first one is to implement a projection-based model order reduction, in the displacement field, and evaluate the speed up of the computational time and the accuracy achieved by the reduced model.

ii) The following objective is to get a better speed up of the computational time by adding a hyper-reduction of the micro-scale problem. This second level of reduction is applied to a judiciously selected set of stress components. An analysis on the accuracy, the stability and the speed up results of the effects of the parameters which appear in this method is developed to determine selection criteria for these parameters.

iii) Finally the third objective is to evaluate the performance of the complete multi-scale algorithm using the hyper-reduction process to solve the micro-scale problem

1.4 Thesis Outline

In what follows, the *Chapter 2* develops the theory of the hyper-reduction of the micro-scale problem. It starts with a description of the multi-scale approach and the homogenisation techniques. Then the Proper Order Reduction techniques, which are the basis of the model order reduction, are introduced. And finally, the hyper-reduction process in two levels is presented.

The *Chapter 3* presents some numerical examples. First, the results of the single-step model order reduction and then the hyper-reduction of the micro-scale problem are analysed to compare the computational accelerations achieved at the micro-scale. Second, two examples of multi-scale problems are studied to evaluate the performances achieved on a whole multi-scale problem by introducing a hyper-reduction of the micro-scale problem.

Chapter 2:

Model Reduction Strategy

2.1 Definition of the mechanical problem

2.1.1 Multi-scale approach

A multi-scale approach can be envisaged when the principle of separation of scales is verified. According to M.G.D. Geers, V.G. Kouznetsova & W.A.M. Brekelmans [8]: "*The microscopic length scale is assumed to be much smaller than the characteristic length over which the macroscopic loading varies in space*", which results in a ranking of the governing length scales: $l_{micro} \ll l_{macro}$,

where l_{micro} and l_{macro} refer to the micro-scale and the macro-scale lengths respectively.

Even when the methodology can be applied to rather general micro-structure topologies, for simplicity, we are considering the existence of a two phase material: a homogeneous material Ω_{μ}^{s} (matrix) with voids Ω_{μ}^{v}, which are periodically distributed into the homogeneous matrix. Thus, we are analyzing the smallest periodic cell which we call the Unit Cell, see *Figure 2.1*.

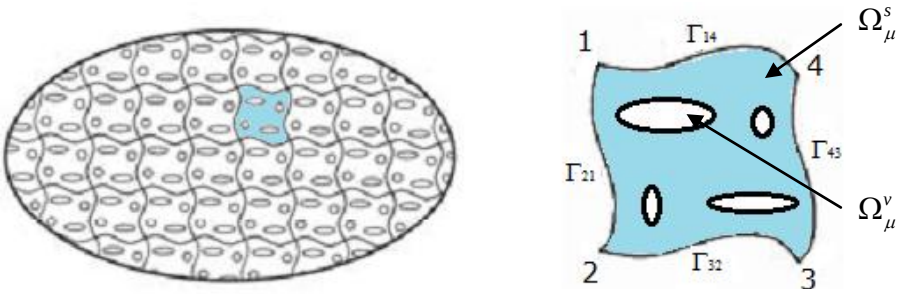

Global Periodicity *Unit Cell*

Figure 2.1 : Periodicity of the micro-structure and Unit Cell

Also, we assume that the void part of the Unit Cell does not intersect the Unit Cell boundary, i.e.: $\bar{\Omega}_\mu^v \bigcap \partial\Omega_\mu = \varnothing$,

where $\bar{\Omega}_\mu^v$ denotes all points in Ω_μ^v plus the limit points of Ω_μ^v, and $\partial\Omega_\mu$ the Unit Cell boundary.

Assuming these conditions, a homogenisation procedure can be used. This procedure can be applied to the resolution of multi-scale problems. In this purpose, the stress tensor for each Gauss point of the mesh at the macroscopic scale will be determined by resolving the micro-scale problem of a Unit Cell submitted to the corresponding input strain. The output data of this micro-scale problem have to be homogenised to be used by the Gauss point analysed at the macroscopic scale. The pattern of the multi-scale resolution process is presented in the Figure 2.2.

The purpose of the *Chapter 2* is to determine a strategy to reduce the micro-scale problem. Two steps of reduction are required to reduce efficiently the computational cost of the multi-scale problem. But before reducing the problem some variables and concept have to be defined in this paragraph 2.1.

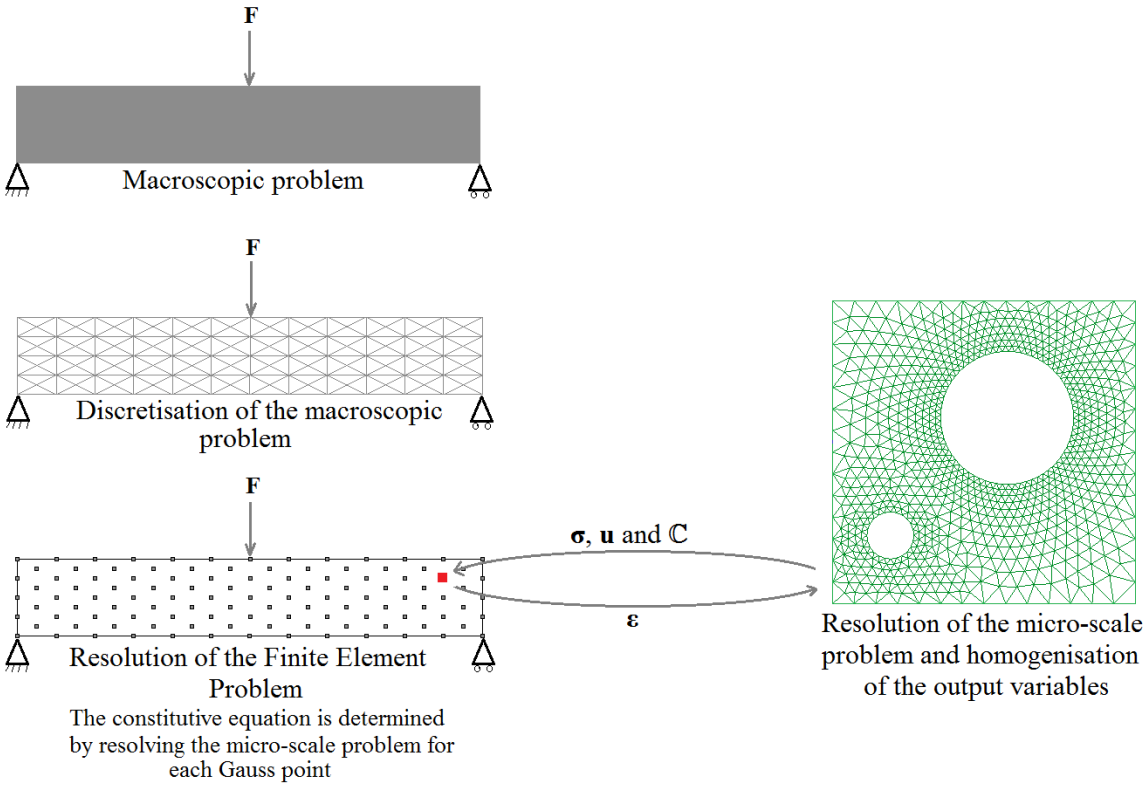

Figure 2.2 : Diagram of resolution of a multi-scale problem

2.1.2 Unit Cell Equilibrium problem and homogenised variables

In this subsection, we present a summary of the homogenization procedure theoretical basis which follows closely the paper of Souza et al (Con Feijoo). Additional details are presented in the reference work.

2.1.2.1 The displacement fluctuation field

Without losing generality of the formulation, any microscopic displacement field $\mathbf{u}_\mu$ can be split into a sum of a homogeneous strain displacement $\boldsymbol{\varepsilon}(t)\mathbf{y}$ (i.e. a displacement that varies linearly in $\mathbf{y}$), and a displacement fluctuation field $\tilde{\mathbf{u}}_\mu$:

$$\mathbf{u}_\mu(\boldsymbol{y},t) = \boldsymbol{\varepsilon}(t)\boldsymbol{y} + \tilde{\mathbf{u}}_\mu(\boldsymbol{y},t)\,, \qquad (1)$$

In the same way the microscopic strain field $\boldsymbol{\varepsilon}_\mu$ is defined as the sum of a homogeneous (constant in $\mathbf{y}$) strain coinciding with the macroscopic strain ε, and a strain fluctuation field:

$$\boldsymbol{\varepsilon}_{\mu}(\boldsymbol{y},t) = \boldsymbol{\varepsilon}(\boldsymbol{x},t) + \tilde{\boldsymbol{\varepsilon}}(\boldsymbol{y},t) = \boldsymbol{\varepsilon}(\boldsymbol{x},t) + \nabla^{s}\tilde{\mathbf{u}}_{\mu}, \qquad (2)$$

2.1.2.2 The homogenised strain tensor

The microscopic strain tensor field $\boldsymbol{\varepsilon}_{\mu}$ is defined as the symmetric gradient of the microscopic displacement field $\mathbf{u}_{\mu}$ of the Unit Cell:

$$\boldsymbol{\varepsilon}_{\mu} = \nabla^{s}\mathbf{u}_{\mu} \qquad (3)$$

At any instant t, the macroscopic strain tensor ε at an arbitrary point x is defined as the volume average of this microscopic strain tensor field, $\boldsymbol{\varepsilon}_{\mu}$, over Ω_{μ}:

$$\boldsymbol{\varepsilon}(t) = \frac{1}{V_{\mu}}\int_{\Omega_{\mu}} \boldsymbol{\varepsilon}_{\mu}(y,t)\,\mathrm{dV}, \qquad (4)$$

where V_{μ} is the volume of the Unit Cell.

2.1.2.3 Unit Cell Equilibrium equation

The equilibrium of the Unit Cell has to be conserved for each instant t of the deformation.

We assume that the Unit Cell is not subjected to body forces or external tractions applied on its external boundary $\partial\Omega_{\mu}$. Then the variational formulation of the Unit Cell equilibrium can be written as:

$$\int_{\Omega_{\mu}} \boldsymbol{\sigma}_{\mu}(\mathbf{y},t) : \nabla^{s}\eta\,\mathrm{dV} = 0, \qquad (5)$$

where $\boldsymbol{\sigma}_{\mu} = \boldsymbol{\sigma}_{\mu}(\mathbf{y},t)$ refers to the microscopic stress.

2.1.2.4 The homogenised stress tensor

At every point **x** of the macro-continuum the macroscopic (or *homogenised*) stress σ is defined as the volume average of the microscopic stress field $\boldsymbol{\sigma}_{\mu}$, over Ω_{μ}:

$$\boldsymbol{\sigma}(\boldsymbol{x},t) \equiv \frac{1}{V_\mu}\int_{\Omega_\mu} \boldsymbol{\sigma}_\mu(\boldsymbol{y},t)\,\mathrm{dV}\,, \tag{6}$$

$$\boldsymbol{\sigma}(\boldsymbol{x},t) = \frac{1}{V_\mu}\int_{\Omega_\mu^s} \boldsymbol{\sigma}_\mu(\boldsymbol{y},t)\mathrm{dV} + \frac{1}{V_\mu}\int_{\Omega_\mu^v} \boldsymbol{\sigma}_\mu(\boldsymbol{y},t)\mathrm{dV}\,, \tag{7}$$

2.1.2.5 The homogenised consistent tangent operator

The consistent tangent operator enables to evaluate the variation of the stress regarding the deformation. It is defined as follows:

$$\mathbb{C}_{ijkl} = \frac{\partial \boldsymbol{\sigma}_{kl}}{\partial \boldsymbol{\varepsilon}_{ij}}\,, \tag{8}$$

$$\mathbb{C} = \frac{\partial \boldsymbol{\sigma}(\boldsymbol{\varepsilon} + \nabla^s \tilde{\mathbf{u}})}{\partial \boldsymbol{\varepsilon}}\,, \tag{9}$$

Similarly to the homogenised strain tensor and the homogenised stress tensor the homogenised consistent tangent operator is defined as the volume average of this microscopic consistent tangent operator, $\mathbb{C}_\mu$, over Ω_μ:

$$\mathbb{C} = \frac{1}{V_\mu}\int_{\Omega_\mu}\left(\frac{\partial \boldsymbol{\sigma}_\mu}{\partial \boldsymbol{\varepsilon}} + \frac{\partial \boldsymbol{\sigma}_\mu}{\partial \nabla^s \tilde{\mathbf{u}}_\mu}.\frac{\partial \nabla^s \tilde{\mathbf{u}}_\mu}{\partial \boldsymbol{\varepsilon}}\right)\mathrm{dV} \tag{10}$$

A numerical perturbation method will be used to evaluate the homogenised tensor over the micro-cell in the case of the hyper-reduced model. After obtaining the homogenised stress tensor $\boldsymbol{\sigma}_\mu$ for a deformation $\boldsymbol{\varepsilon}_\mu$ we solve again three times the microscopic problem introducing three perturbations $\Delta\boldsymbol{\varepsilon}_x$, $\Delta\boldsymbol{\varepsilon}_y$ and $\Delta\boldsymbol{\gamma}_{xy}$ to obtain the three stress tensors corresponding: $\boldsymbol{\sigma}_x^*$, $\boldsymbol{\sigma}_y^*$ and $\boldsymbol{\sigma}_{xy}^*$. Then the homogenised consistent tangent tensor for the micro-cell is built as follows:

$$\mathbb{C}_\mu = \left[\begin{array}{c|c|c|c} \dfrac{\boldsymbol{\sigma}_\mu - \boldsymbol{\sigma}_x^*}{\Delta\boldsymbol{\varepsilon}_x} & \dfrac{\boldsymbol{\sigma}_\mu - \boldsymbol{\sigma}_y^*}{\Delta\boldsymbol{\varepsilon}_y} & \begin{array}{c}0\\0\\0\\0\end{array} & \dfrac{\boldsymbol{\sigma}_\mu - \boldsymbol{\sigma}_{xy}^*}{\Delta\boldsymbol{\gamma}_{xy}} \end{array}\right] \tag{11}$$

2.1.3 Finite Element Analysis

The Finite Element formulation developed is based on the Principle of Virtual Work, which states that the total virtual work done by all the forces acting on a system in static equilibrium in zero for a set of infinitesimal virtual displacements from equilibrium.

Considering that a body force field $\mathbf{b}$ and an external traction field $\mathbf{t}^e$ act on the solid, the principle of virtual work can be written for a 2D problem as follows:

$$\int_\Omega \delta\boldsymbol{\varepsilon}^T \cdot \boldsymbol{\sigma}\, \mathrm{d}\Omega = \int_\Omega \delta\mathbf{u}^T \cdot \mathbf{b}\, \mathrm{d}\Omega + \int_\Gamma \delta\mathbf{u}^T \cdot \mathbf{t}^e\, \mathrm{d}\Gamma, \quad \forall \delta\mathbf{u} \text{ admissible} \tag{12}$$

The finite element method will be used to solve the problem at the micro-scale (noted "*micro-cell problem*"). This micro-cell has boundary conditions which ensure its periodicity. The input of the micro-scale problem is the stain tensor arising on the corresponding Gauss point of the macro-scale mesh. The main output is the fluctuations required to keep the micro-cell in equilibrium under this constraint. Thus, in this case, the body force field $\mathbf{b}$ and the external traction field $\mathbf{t}^e$ produce null virtual work, i.e. they are orthogonal to the space of the virtual displacements fluctuations (after considering the Hill-Mandel principle)and the equation (12) becomes:

$$\int_\Omega \delta\boldsymbol{\varepsilon}_\mu^T \cdot \boldsymbol{\sigma}\, \mathrm{d}\Omega = 0, \tag{13}$$

Similarly to the equation (1) the microscopic strain tensor $\boldsymbol{\varepsilon}_\mu$ is the sum of the macroscopic strain tensor acting on the Gauss point and the perturbations of the micro-cell due to the macroscopic strain tensor:

$$\boldsymbol{\varepsilon}_\mu(\boldsymbol{y},t) = \boldsymbol{\varepsilon}_{macro}(\boldsymbol{x},t) + \tilde{\boldsymbol{\varepsilon}}_\mu(\boldsymbol{y},t), \tag{14}$$

According to the finite element theory a relationship is made between stress, strain and displacement:

$$\boldsymbol{\varepsilon} = \mathbf{B}\mathbf{u}, \tag{15}$$

$$\boldsymbol{\sigma} = \mathbb{C}\boldsymbol{\varepsilon}, \tag{16}$$

where **B** denotes the strain-displacement matrix and $\mathbb{C}$ is the consistent tangent operator.

Using the relationships (15) and (16) the equation (13) can be rewritten:

$$\int_{A^e} \left\{\delta \mathbf{u}_\mu^e\right\}^T \mathbf{B}_\mu{}^T \mathbb{C}_\mu^e \mathbf{B}_\mu \left\{\delta \mathbf{u}_\mu^e\right\} dA = 0, \qquad \textbf{(17)}$$

i.e.

$$\left\{\delta \mathbf{u}_\mu^e\right\}^T \mathbf{K}_\mu^e \left\{\delta \mathbf{u}_\mu^e\right\} = 0 \qquad \textbf{(18)}$$

where the element stiffness matrix is defined as:

$$\mathbf{K}_\mu^e = \int_{A^e} \mathbf{B}_\mu{}^T . \mathbb{C}_\mu^e . \mathbf{B}_\mu \, dA. \qquad \textbf{(19)}$$

The integrations over the elements of the micro-cell are performed numerically using the Gaussian quadrature in the Matlab code developed.

2.2 Proper Orthogonal Decomposition (POD)

The model order reduction process developed is based on the Proper Orthogonal Decomposition (POD). These methods aim to find a basis for the modal decomposition of an ensemble of data.

The three main POD algorithms are the Principal Component Analysis (PCA), the Karhunen-Loève Decomposition (KLD) and the Singular Value Decomposition (SVD). This last one will be used twice in the reduction process to obtain the reduced basis vectors from the snapshots matrices.

Initially developed for real-square matrices, the SVD is nowadays established for general non-squares matrices.

Let $\mathbf{X} = [\mathbf{x}_1, ..., \mathbf{x}_n]$ be a m x n matrix, with $m \leq n$ and $\mathbf{x}_j \in \mathbb{R}^m$, of rank $d \leq m$. Arranging in decreasing order the singular values $\boldsymbol{\sigma}_i$ of $\mathbf{X}^T$: $\sigma_1 \geq \sigma_2 \geq ... \geq \sigma_d > 0$ the SVD ensures the existence of orthogonal matrices $\boldsymbol{\Phi} = \begin{bmatrix} \boldsymbol{\varphi}_1 & ... & \boldsymbol{\varphi}_m \end{bmatrix} \in \mathbb{R}^{m \times m}$ and $\mathbf{V} = \begin{bmatrix} \mathbf{v}_1 & ... & \mathbf{v}_n \end{bmatrix} \in \mathbb{R}^{n \times n}$ such that:

$$\mathbf{X} = \Phi . \boldsymbol{\Sigma} . \mathbf{V}^T \qquad (20)$$

$$\mathbf{X} = \underbrace{\begin{bmatrix} \boldsymbol{\varphi}_1 & ... & \boldsymbol{\varphi}_m \end{bmatrix}}_{m \times m} . \begin{bmatrix} \mathbf{q}_1{}^T \\ \vdots \\ \vdots \\ \mathbf{q}_m{}^T \end{bmatrix}_{m \times n} \quad with\ (\mathbf{q}_1, ..., \mathbf{q}_m) \in \mathbb{R}^n \qquad (21)$$

The columns of $\boldsymbol{\Phi}$ and $\mathbf{V}$ are respectively the eigenvectors of the matrices $\mathbf{X}\mathbf{X}^T$ and $\mathbf{X}^T\mathbf{X}$.

For a given $k < d$ the orthogonal basis vector that best approximates $\mathbf{X}$ is $\{\boldsymbol{\varphi}_1, \quad ... \quad , \boldsymbol{\varphi}_k\}$, named the *POD basis of rank k.*

The error of the approximate function using this POD basis is given by:

$$\sum_{j=1}^{n}\left\|\mathbf{x}_i-\sum_{i=1}^{k}(\mathbf{x}_j{}^T\boldsymbol{\varphi}_i)\boldsymbol{\varphi}_i\right\|_2^2=\sum_{i=k+1}^{d}\sigma_i{}^2=\sum_{i=k+1}^{d}\lambda_i \qquad (22)$$

(Volkwein [11]).

Thus, inasmuch as the snapshot matrix of data describes the whole general space, the POD method makes it possible to determine an accurate reduced basis. In what follows the POD method will be used to determine the displacements modes in the first Model Order Reduction (2.3) and the stress modes in the hyper-reduction of the micro-scale model (2.4).

2.3 Model order reduction of the micro-scale problem

The idea of the model order reduction is to work in a reduced-space to decrease the size of the system and therefore decrease the computational cost of resolution of the micro-scale problem.

This reduction technique is composed of two parts. The *offline part* contains the determination of the reduced basis and the computation of the strain-displacement matrix. These calculations are isolated because they just need to be performed once in the process and do not depend of the macroscopic strain imposed on the micro-cell. Then the *online part* is the resolution of the problem.

2.3.1 Construction of a reduced displacement basis $\boldsymbol{\Phi}$

The first step of the model order reduction is to build a reduced displacement basis $\boldsymbol{\Phi}=\left\{\boldsymbol{\varphi}_1,\ \ldots\ ,\boldsymbol{\varphi}_{n_{\hat{u}}}\right\}$ of rank $n_{\hat{u}}$ which will be used like a map between the general space and the reduced displacement space. This construction is performed *offline*. The rank $n_{\hat{u}}$ of $\boldsymbol{\Phi}$ is chosen to conserve the most important displacement modes.

The displacement vector $\mathbf{u}$ is recovered from the reduced displacement $\hat{\mathbf{u}}$ using the following relationship:

$$\underset{n_{dof}^{total}\ x1}{\mathbf{u}} = \underset{n_{dof}^{total}\ x\ n_{\hat{\mathbf{u}}}}{\boldsymbol{\Phi}}\ \underset{n_{\hat{\mathbf{u}}}\ x1}{\hat{\mathbf{u}}} \qquad (23)$$

To create the snapshot matrix of displacements necessary for the determination of the reduced basis, the classical Finite Element code is run imposing a given strain path. The choice of this "training" path is a crucial factor in constructing the reduced basis. Indeed the snapshot matrix has to be able to capture any strain path during the online process. The training path used for the 2D problems studied in this thesis is composed of load/unload functions including an inelastic part, in three directions of the strain space $\boldsymbol{\varepsilon}_1 = \begin{bmatrix} \varepsilon_x & 0 & 0 \end{bmatrix}$, $\boldsymbol{\varepsilon}_2 = \begin{bmatrix} 0 & \varepsilon_y & 0 \end{bmatrix}$ and $\boldsymbol{\varepsilon}_3 = \begin{bmatrix} 0 & 0 & \gamma_{xy} \end{bmatrix}$.

This part of construction of the reduced basis is common to the two model order reduction processes presented in the paragraphs 2.3.2 and 2.3.3.

2.3.2 "Phi-K-Phi" model

This first implemented model order reduction uses the reduced space in the *online part* of the process. The *offline* computation of the strain-displacement matrix $\mathbb{B}$ is carried out without using the reduced basis. The name of this model comes from the calculation of the stiffness matrix during the *online part*.

- *Calculation of the strain-displacement matrix*

The strain-displacement matrix $\mathbb{B}$ is composed of sub-matrices $\mathbb{B}^{(i)}$ for all integration points and assembled as follows:

$$\mathbb{B} = \begin{bmatrix} \mathbb{B}^{(1)} \\ \mathbb{B}^{(2)} \\ \vdots \\ \mathbb{B}^{(NPG)} \end{bmatrix} \qquad (24)$$

Each $\mathbb{B}^{(i)}$ sub-matrix is deduced from the elemental strain-displacement matrix $\mathbf{B}^e$, Jacobian matrix $\mathbf{J}^e$ and volume V^e multiplied by the weight factor of the Gauss point $w^{(i)}$. These sub-matrices are composed of as many lines as the number of components (in the Voigt notation) of the Cauchy stress tensor n_{tens} and the number of columns is equal to the total number of degrees of freedom.

$$\underset{n_{tens}\ x\ n_{dof\ total}}{\mathbb{B}^{(i)}} = w^{(i)}\,\mathbf{B}^{e}\,\mathbf{J}^{e}\,V^{e} \qquad (25)$$

- *Online part*

The *online part* consists in the proper resolution of the micro-scale problem.

Considering its geometry and its material properties the *online part* aims to determine the behaviour of the micro-cell under the macroscopic strain imposed.

The first step of the resolution is the computation of the internal force vector using the strain-displacement tensor $\mathbb{B}$ calculated in the *offline part* and the stress tensor assembled as follows:

$$\mathbb{S} = \begin{bmatrix} \boldsymbol{\sigma}^{(1)} \\ \boldsymbol{\sigma}^{(2)} \\ \vdots \\ \boldsymbol{\sigma}^{(NPG)} \end{bmatrix} \quad \text{where } \boldsymbol{\sigma}^{(i)} = \begin{Bmatrix} \sigma_x^{(i)} \\ \sigma_y^{(i)} \\ \sigma_z^{(i)} \\ \gamma_{xy}^{(i)} \end{Bmatrix} \text{ in the Voigt notation.} \qquad (26)$$

Thus the internal force vector $\mathbf{f}^{\text{int}}$ is written:

$$\mathbf{f}^{\text{int}} = \mathbb{B}^{T}\mathbb{S} \qquad (27)$$

The reduced internal force vector is obtained multiplying $\mathbf{f}^{\text{int}}$ by the reduced displacement basis:

$$\underset{n_{\hat{\mathbf{u}}}\ x1}{\hat{\mathbf{f}}^{\text{int}}} = \underset{n_{\hat{\mathbf{u}}}\ x\ n_{dof\ total}}{\boldsymbol{\Phi}^{T}}\ \underset{n_{dof\ total}\ x1}{\mathbf{f}^{\text{int}}} \qquad (28)$$

This model requires the computation of the full stiffness matrix $\mathbf{K}$ of the micro-cell. This matrix is assembled from the element stiffness matrices $\mathbf{K}^{e}$.

$$\mathbf{K}^e = \mathbf{B}^T \mathbb{C}^e \mathbf{B} \quad (29)$$

$$\mathbf{K} = \mathop{\mathbb{A}}_{e=1}^{n_{elem}} \mathbf{K}^e \quad (30)$$

where $\mathop{\mathbb{A}}_{e=1}^{n_{elem}}$ denotes the assembly process and n_{elem} the number of element in the micro-cell.

The reduced stiffness matrix $\hat{\mathbf{K}}$ is calculated afterward using the reduced displacement basis:

$$\underset{n_{\hat{\mathbf{u}}} \, x \, n_{\hat{\mathbf{u}}}}{\hat{\mathbf{K}}} = \mathbf{\Phi}^T \underset{n_{dof}^{total} \, x \, n_{dof}^{total}}{\mathbf{K}} \mathbf{\Phi} \quad (31)$$

Thus, rewriting the equation (18), the system of equations to solve becomes:

$$\underset{1 x n_{\hat{\mathbf{u}}}}{\{\hat{\mathbf{u}}\}^T} \underset{n_{\hat{\mathbf{u}}} x n_{\hat{\mathbf{u}}}}{\hat{\mathbf{K}}} \underset{n_{\hat{\mathbf{u}}} x 1}{\{\hat{\mathbf{u}}\}} = 0 \quad (32)$$

The iterative Newton-Raphson algorithm is applied to solve numerically this reduced micro-scale problem. At each iteration a displacement increment $\Delta\hat{\mathbf{u}}$ is added to the displacement guess to get closer to the exact solution.

$$\hat{\mathbf{u}}^{k+1} = \hat{\mathbf{u}}^k + \Delta\hat{\mathbf{u}}^{k+1} \quad (33)$$

where

$$\Delta\hat{\mathbf{u}}^{k+1} = -\left[\hat{\mathbf{K}}^k\right]^{-1} . \left[\mathbf{res}^k\right] \quad (34)$$

and $\left[\mathbf{res}^k\right]$ is the residual for the iteration *k*.

This iterative method ensures a quadratic convergence to the solution.

A drawback of this first model order reduction is that it is necessary to calculate the full strain-displacement matrix and the full stiffness matrix. The reduction is only applied after performing these costly calculations.

2.3.3 "$\hat{\mathbf{B}}$" model

The name of this second model order reduction process comes from the fact that, contrary to the first one, this model uses a *reduced* strain-displacement matrix. Thus the calculation of the stiffness matrix is directly performed in the reduced space and does not require calculating the full stiffness matrix. The *offline part* as well as the *online part* of these two models is different. Nevertheless the offline construction of the reduced displacement basis $\boldsymbol{\Phi} = \left\{ \boldsymbol{\varphi}_1, \quad ... \quad , \boldsymbol{\varphi}_{n_{\hat{\mathbf{u}}}} \right\}$ is unchanged.

- *Calculation of the reduced strain-displacement matrix*

The reduced element strain-displacement matrix $\hat{\mathbf{B}}^e$ is derived from the element strain-displacement matrix $\mathbf{B}^e$ using the sub-matrix of the reduced displacement basis $\boldsymbol{\Phi}$ corresponding to the degrees of freedom of the element, denoted $\boldsymbol{\Phi}^e$.

$$\underset{n_{tens} \, x \, n_{\hat{\mathbf{u}}}}{\hat{\mathbf{B}}^e} = \underset{n_{tens} \, x \, n_{\mathbf{u}^e}}{\mathbf{B}^e} \; \underset{n_{\mathbf{u}^e} \, x \, n_{\hat{\mathbf{u}}}}{\boldsymbol{\Phi}^e} \qquad \textbf{(35)}$$

where $n_{\hat{\mathbf{u}}}$ is the rank of $\boldsymbol{\Phi}$ and $n_{\mathbf{u}^e}$ is the number of degrees of freedom of the element.

- *Online part*

The input data of the *online part* are the same as the first model order reduction, except the strain-displacement matrix which is now reduced directly in the *offline part*.

Another relevant difference is the assembly process of the internal force vector and the stiffness matrix. Indeed the element matrices and the global matrix have now the same dimensions and the assembly consists in a sum of the elemental contributions.

Thus the internal force vector is given by:

$$\underset{n_{\hat{\mathbf{u}}} \, x1}{\hat{\mathbf{f}}^{\text{int}}} = \mathop{\mathbb{A}}_{e=1}^{n_{elem}} \left\{ \hat{\mathbf{f}}^{\text{int}} \right\}^e = \sum_{e=1}^{n_{elem}} \underset{n_{\hat{\mathbf{u}}} \, x1}{\left\{ \hat{\mathbf{f}}^{\text{int}} \right\}^e} \qquad \textbf{(36)}$$

$$\left\{ \hat{\mathbf{f}}^{\text{int}} \right\}^e = \int_{V^e} \left[\hat{\mathbf{B}}^e \right]^T \boldsymbol{\sigma}^e \, dV \cong \sum_{i_{PG}=1}^{n_{PG}} w^{(i_{PG})} \left[\hat{\mathbf{B}}^e_{i_{PG}} \right]^T \boldsymbol{\sigma}^e_{i_{PG}} . |\, \mathbf{J}^e_{i_{PG}} \,| . V^e \qquad \textbf{(37)}$$

where

Similarly the stiffness matrix of the micro-cell is:

$$\underset{n_{\hat{\mathbf{u}}} x n_{\hat{\mathbf{u}}}}{\hat{\mathbf{K}}} = \mathop{\mathbb{A}}_{e=1}^{n_{elem}} \hat{\mathbf{K}}^e = \sum_{e=1}^{n_{elem}} \underset{n_{\hat{\mathbf{u}}} x n_{\hat{\mathbf{u}}}}{\hat{\mathbf{K}}^e} \qquad \textbf{(38)}$$

where the element stiffness matrices $\hat{\mathbf{K}}^e$ are deduced from the element reduced strain-displacement matrices and the element consistent tangent operators by a relationship similar to the expression (29).

Finally the reduced system to solve is the same than in the previous model:

$$\underset{1 x n_{\hat{\mathbf{u}}}}{\{\hat{\mathbf{u}}\}^T} \; \underset{n_{\hat{\mathbf{u}}} x n_{\hat{\mathbf{u}}}}{\hat{\mathbf{K}}} \; \underset{n_{\hat{\mathbf{u}}} x 1}{\{\hat{\mathbf{u}}\}} = 0 \qquad \textbf{(39)}$$

In the same way it is solved using the iterative Newton-Raphson method.

As stated before this second model has the advantage to directly calculate the reduced stiffness matrix and so save the cost of the computation of the full matrix and its multiplication by the reduction matrix $\boldsymbol{\Phi}$. But as the number of displacement modes $n_{\hat{\mathbf{u}}}$ increases the size of the element stiffness matrices also increases and the saving done can be lost because the computation of the element matrices becomes more expensive, that is why the method “Phi-K-Phi” presented in the paragraph 2.3.2 will be used in the complete reduction algorithm instead of the this second model order reduction named “$\hat{\mathrm{B}}$”.

It is important to notice that working in the reduced displacement space implies losing the locality of the information. Each component of the reduced displacement vector is no longer directly linked to a real degree of freedom, which makes it more difficult to apply non-zero boundary conditions. In this thesis only zero boundary conditions have been studied for the micro-scale problem.

2.4 Hyper-reduction of the micro-scale problem

Because of the disappointing results of the two model order reduction methods present in the paragraph 2.3 other reduction techniques have to be used to decrease the computational cost of the multi-scale problem. Thus a hyper-reduction of the micro-scale problem is performed.

2.4.1 Construction of reduced displacement and stress bases

The first step of this new model is to build a reduced displacement basis $\mathbf{\Phi}_u$ and a reduced stress basis $\mathbf{\Phi}_\sigma$.

Similarly to the two precedent models the classical Finite Element algorithm is run for a given path strain to generate the snapshot matrix of displacement $\mathbf{X}_u$.

Then the "Phi-K-Phi" model order reduction is applied for a path strain and a chosen dimension $n_{\hat{u}}$ of truncated displacement basis in order to generate the stress snapshot matrix $\mathbf{X}_\sigma$. A perturbation force is introduced to capture a trajectory of the stress $\boldsymbol{\sigma}(\boldsymbol{\varepsilon})$ close to the equilibrium but not exactly on it to try to avoid singularity, later on, in the *online part* which used this matrix $\mathbf{X}_\sigma$.

The problem to solve becomes:

$$\int_\Omega \mathbf{B}^T \cdot \boldsymbol{\sigma}\, d\Omega = \mathbf{f} \neq \mathbf{0} \qquad (40)$$

The perturbation force is controlled by the parameter η. For each snapshot *i* the force vector is computed as follows:

$$\mathbf{f}_i^{ext}(\boldsymbol{\varepsilon}) = \eta \int_\Omega \mathbf{B}^{\mathbf{II}^T} \cdot \boldsymbol{\sigma}(\boldsymbol{\varepsilon}^{\mathbf{I}})\, dV = \eta \int_\Omega \underbrace{\mathbf{B}^{\mathbf{II}^T}}_{\mathbf{B}^{\mathbf{I}}\mathbf{\Phi}_u} \cdot \mathrm{E}.\mathbf{B}^{\mathbf{I}} \cdot (1 - \mathbf{\Phi}_u \mathbf{\Phi}_u^T) \cdot \underbrace{\mathbf{u}_i^{\mathbf{I}}(\boldsymbol{\varepsilon})}_{[\mathbf{X}_u]_i}\, dV \qquad (41)$$

where the indication "I" refers to the classical FE model without model order reduction and "II" corresponds to the reduced model "Phi-K-Phi". This construction of the perturbation force implies the use of the same number of snapshot for the generation of the stress snapshot matrix as used for the generation of the displacement snapshot matrix

The displacement and stress bases are obtained from the snapshot matrices $\mathbf{X}_u$ and $\mathbf{X}_\sigma$ using the Proper Orthogonal Decomposition presented in the paragraph 2.2. The choice of the dimensions $n_{\hat{\mathbf{u}}}$ and $n_{\boldsymbol{\sigma}}$ of the truncated bases is important to avoid future singularity in the resolution of the problem. Some relationships to respect between these dimensions are determined in the paragraph 2.4.4.

2.4.2 Strategies of selection of stress tensor components

The hyper-reduction strategy is based on the Gappy Data Reconstruction which makes it possible to obtain the result of the complete stress tensor from the computation results of a set of selected elements of the microscopic mesh. Two different strategies have been developed to select the stress tensor components which enable to reconstruct accurately the full stress tensor. This selection is done *offline*.

2.4.2.1 Greedy Algorithm adapted to Gappy Data Reconstruction

The first one is based on the Greedy algorithm. The principle is to make, at each iteration, the locally optimal choice with the aim to approach the global optimum.

The idea of use this iterative procedure has been proposed by K.Carlberg, C.Bou-Mosleh & C. Farhat [4]. They applied it in order to select the appropriate components to reduce the residual and the Jacobian matrix. Thus the procedure implemented in our case is quite different, even though it is based on the same concept.

The criterion of selection of the elements is the minimization of the error in the projection in the stress space reconstructed using the reduced stress basis. For each iteration i the component of maximum value is looked for in the difference vector between the stress mode $\boldsymbol{\varphi}_{\boldsymbol{\sigma}}^{(i)}$ and its projection $\boldsymbol{\varphi}_{\boldsymbol{\sigma}}^{(i)}$ in the space formed by the projections of the modes $\left\{\hat{\boldsymbol{\varphi}}_{\boldsymbol{\sigma}}^{(1)},...,\hat{\boldsymbol{\varphi}}_{\boldsymbol{\sigma}}^{(i-1)}\right\}$.

It is important to notice that, contrary to the case of reduction of the residual and Jacobian matrix studied by Carlberg, as soon as one stress component of one Gauss point of an element has been selected by this Greedy algorithm all the components of

this element have to be added to the sample stress components list. This requirement is imposed by the Gappy Data Reconstruction implementation.

2.4.2.2 POD Reconstruction-based algorithm

The second selection algorithm is based on the POD reconstruction error minimisation.

The Proper Orthogonal Decomposition provides three matrices $\mathbf{\Phi}$, $\mathbf{\Sigma}$ and $\mathbf{V}$ which enables to approximate the snapshot matrix.

$$\bar{\bar{\mathbf{X}}}_{\boldsymbol{\sigma}} = \begin{bmatrix} \bar{\bar{\mathbf{X}}}_{\boldsymbol{\sigma}}^{(1)} \\ \vdots \\ \bar{\bar{\mathbf{X}}}_{\boldsymbol{\sigma}}^{(n_{tens} \, x \, n_{PG})} \end{bmatrix} \cong \sum_{k=1}^{n_{\boldsymbol{\sigma}}} \sigma_k \boldsymbol{\varphi}_k \mathbf{V}_k^T \qquad \textbf{(42)}$$

As the dimension $n_{\boldsymbol{\sigma}}$ of the reduced stress basis becomes closer to the rank d of the stress snapshot matrix $\mathbf{X}_{\boldsymbol{\sigma}}$ this approximation $\bar{\bar{\mathbf{X}}}_{\boldsymbol{\sigma}}$ tends to be exact.

For each component i of the stress tensor the error $\mathbf{e}^i$ is computed:

$$\mathbf{e}^i = \mathbf{X}_{\boldsymbol{\sigma}}{}^i - \bar{\bar{\mathbf{X}}}_{\boldsymbol{\sigma}}{}^i \qquad \textbf{(43)}$$

where $\mathbf{X}_{\boldsymbol{\sigma}}{}^i$ and $\bar{\bar{\mathbf{X}}}_{\boldsymbol{\sigma}}{}^i$ correspond respectively to the i^{th} lines of the exact and approximated stress snapshot matrices.

This algorithm looks for the $n_{\sigma *}$ indices of stress components which provide the smallest error. They correspond to the best reconstructed lines of the stress snapshot matrix by the Proper Order Decomposition.

The *Figure 2.3* presents the evolution of the POD reconstruction error for various dimension n_{σ} of truncated stress space. The abscissas of the graphics are the number of the Gauss points. They have been renumbered from the Gauss point which deals with the smallest POD reconstruction error to the Gauss point encountering the higher error. When the number n_{σ} of stress modes used in the approximation of $\mathbf{X}_{\boldsymbol{\sigma}}$ is small the gradient of the distribution of the error is higher than for high n_{σ}. That means that this criterion is more selective when few stress modes are chosen.

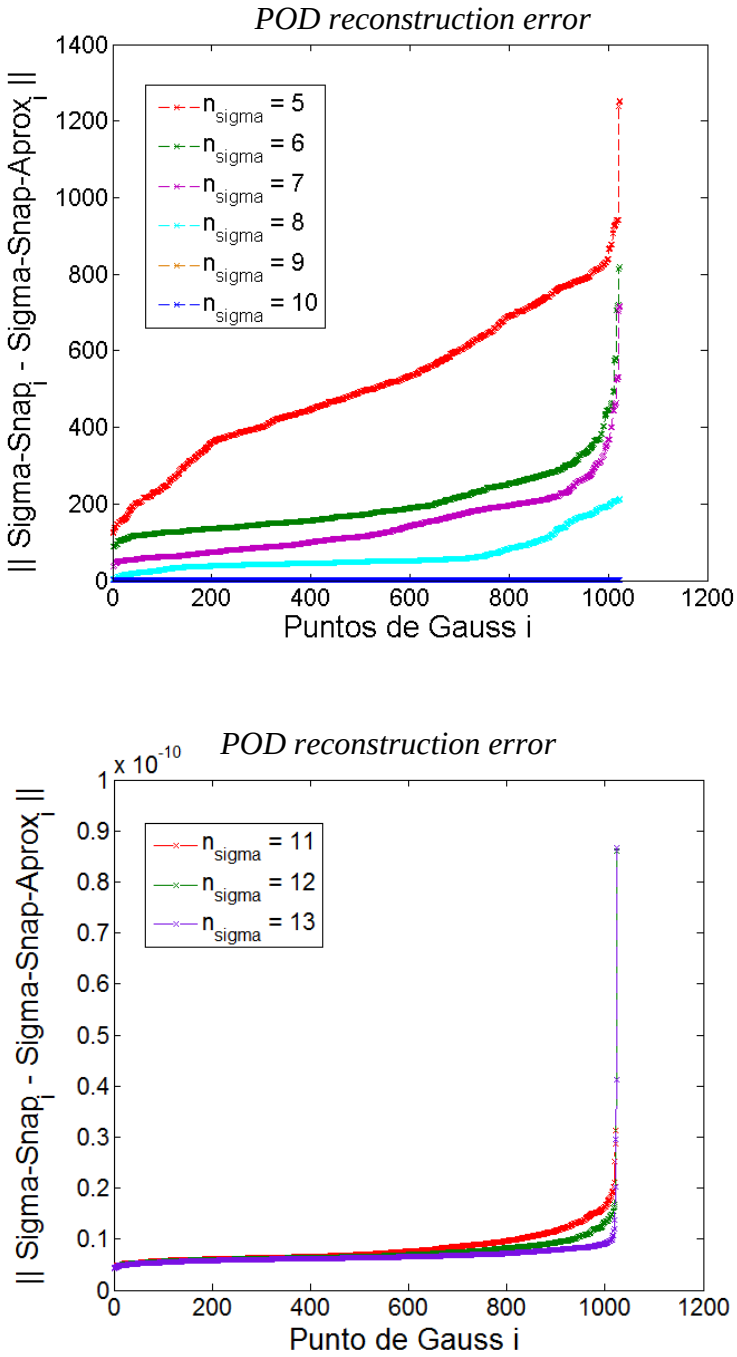

Figure 2.3 : Variation of the POD reconstruction error distribution according to n_σ

As for the Greedy algorithm when one Gauss point is selected by this algorithm all components of all Gauss points of the element are selected in the sample list of stress components used in the Gappy Data Reconstruction.

2.4.3 Gappy Data Reconstruction

The hyper-reduction is based on the Gappy Data Reconstruction method. It is a technique, mathematically equivalent to a least-squares regression in one discrete variable, to reconstruct an incomplete set of data using some experimental and additional computational known data. Within the framework of the model order reduction it aims to approximate the results of all elements from the computational results of some selected elements and a reduced basis.

A judicious selection of n_{σ^*} components of the stress vector $\mathbb{S} = \left[\boldsymbol{\sigma}^{(1)} \quad \boldsymbol{\sigma}^{(2)} \quad \cdots \quad \boldsymbol{\sigma}^{(n_{PG})} \right]^T$ is performed using one of the two algorithms presented in the paragraph 2.4.2. Thus the stress tensor can be split into two sub-vectors: $\mathbb{S}^* \in \mathbb{R}^{n_{\sigma^*} x1}$ which corresponds to the selected components and $\tilde{\mathbb{S}} \in \mathbb{R}^{((n_{tens} x n_{PG}) - n_{\sigma^*}) x1}$ which will be deduced from $\mathbb{S}^*$. The reduced stress basis $\boldsymbol{\Phi}_{\boldsymbol{\sigma}} \in \mathbb{R}^{(n_{tens} x n_{PG}) x n_{\boldsymbol{\sigma}}}$ is decomposed similarly into $\boldsymbol{\Phi}_{\boldsymbol{\sigma}^*} \in \mathbb{R}^{n_{\boldsymbol{\sigma}^*} x n_{\boldsymbol{\sigma}}}$ and $\boldsymbol{\Phi}_{\tilde{\boldsymbol{\sigma}}} \in \mathbb{R}^{((n_{tens} x n_{PG}) - n_{\boldsymbol{\sigma}^*}) x n_{\boldsymbol{\sigma}}}$.

$$\mathbb{S} = \begin{bmatrix} \tilde{\mathbb{S}} \\ — \\ \mathbb{S}^* \end{bmatrix} \qquad \boldsymbol{\Phi}_{\boldsymbol{\sigma}} = \begin{bmatrix} \boldsymbol{\Phi}_{\tilde{\boldsymbol{\sigma}}} \\ — \\ \boldsymbol{\Phi}_{\boldsymbol{\sigma}^*} \end{bmatrix} \tag{44}$$

The numerical integration of the constitutive equation is only performed at the Gauss Point corresponding to the selected elements and provides the part $\mathbb{S}^* \in \mathbb{R}^{n_{\sigma^*} x1}$ of the stress tensor. The complementary part $\tilde{\mathbb{S}}$ is deduced as follows:

$$\mathbb{S} = \begin{bmatrix} \tilde{\mathbb{S}} \\ — \\ \mathbb{S}^* \end{bmatrix} \cong \begin{bmatrix} \boldsymbol{\Phi}_{\tilde{\boldsymbol{\sigma}}} \\ — \\ \boldsymbol{\Phi}_{\boldsymbol{\sigma}^*} \end{bmatrix} \hat{\boldsymbol{\sigma}} \overset{denoted}{\equiv} \begin{bmatrix} \tilde{\mathbb{S}}_R \\ — \\ \mathbb{S}^*_R \end{bmatrix} \tag{45}$$

thus

$$\mathbb{S}^* \cong \mathbb{S}^*_R = \boldsymbol{\Phi}_{\boldsymbol{\sigma}^*} \hat{\boldsymbol{\sigma}} \tag{46}$$

$$\boldsymbol{\Phi}^T_{\boldsymbol{\sigma}^*} \mathbb{S}^*_R = (\boldsymbol{\Phi}^T_{\boldsymbol{\sigma}^*} \boldsymbol{\Phi}_{\boldsymbol{\sigma}^*}) \hat{\boldsymbol{\sigma}} \tag{47}$$

$$\hat{\boldsymbol{\sigma}} = (\boldsymbol{\Phi}_{\boldsymbol{\sigma}^*}^T \boldsymbol{\Phi}_{\boldsymbol{\sigma}^*})^{-1} \boldsymbol{\Phi}_{\boldsymbol{\sigma}^*}^T \mathbb{S}_R^* \quad (48)$$

$$\underset{(n_{tens}\, x\, n_{PG})\, x 1}{\mathbb{S}_R} = \begin{bmatrix} \tilde{\mathbb{S}}_R \\ — \\ \mathbb{S}_R^* \end{bmatrix} = \underbrace{\begin{bmatrix} \boldsymbol{\Phi}_{\tilde{\boldsymbol{\sigma}}} \\ — \\ \boldsymbol{\Phi}_{\boldsymbol{\sigma}^*} \end{bmatrix}}_{(n_{tens}\, x\, n_{PG})\, x\, n_{\boldsymbol{\sigma}}} \underbrace{(\boldsymbol{\Phi}_{\boldsymbol{\sigma}^*}^T \boldsymbol{\Phi}_{\boldsymbol{\sigma}^*})^{-1} \boldsymbol{\Phi}_{\boldsymbol{\sigma}^*}^T \mathbb{S}_R^*}_{n_{\boldsymbol{\sigma}}\, x 1} = \underbrace{\begin{bmatrix} \boldsymbol{\Phi}_{\tilde{\boldsymbol{\sigma}}} (\boldsymbol{\Phi}_{\boldsymbol{\sigma}^*}^T \boldsymbol{\Phi}_{\boldsymbol{\sigma}^*})^{-1} \boldsymbol{\Phi}_{\boldsymbol{\sigma}^*}^T \\ — \\ \boldsymbol{\Phi}^* (\boldsymbol{\Phi}_{\boldsymbol{\sigma}^*}^T \boldsymbol{\Phi}_{\boldsymbol{\sigma}^*})^{-1} \boldsymbol{\Phi}_{\boldsymbol{\sigma}^*}^T \end{bmatrix}}_{(n_{tens}\, x\, n_{PG})\, x\, n_{\boldsymbol{\sigma}^*}} \underbrace{\mathbb{S}_R^*}_{n_{\boldsymbol{\sigma}^*} x 1} \quad (49)$$

which can be rewritten:

$$\underset{(n_{tens}\, x\, n_{PG})\, x 1}{\mathbb{S}_R} = \underset{(n_{tens}\, x\, n_{PG})\, x\, n_{\sigma^*}}{\mathbb{A}_\sigma} \; \underset{n_{\sigma^*} x 1}{\mathbb{S}_R^*} \quad (50)$$

where $$\mathbb{A}_{\boldsymbol{\sigma}} = \begin{bmatrix} \boldsymbol{\Phi}_{\tilde{\boldsymbol{\sigma}}} (\boldsymbol{\Phi}_{\boldsymbol{\sigma}^*}^T \boldsymbol{\Phi}_{\boldsymbol{\sigma}^*})^{-1} \boldsymbol{\Phi}_{\boldsymbol{\sigma}^*}^T \\ — \\ \boldsymbol{\Phi}_{\boldsymbol{\sigma}^*} (\boldsymbol{\Phi}_{\boldsymbol{\sigma}^*}^T \boldsymbol{\Phi}_{\boldsymbol{\sigma}^*})^{-1} \boldsymbol{\Phi}_{\boldsymbol{\sigma}^*}^T \end{bmatrix} \in \mathbb{R}^{(n_{tens}\, x\, n_{PG})\, x\, n_{\boldsymbol{\sigma}^*}} \quad (51)$$

The Gappy Data Reconstruction makes it possible to reconstruct exactly the part $\tilde{\mathbb{S}}_R$ of the stress vector from the computed part $\mathbb{S}_R^*$ as long as the complete rank of the matrix $\mathbb{A}_\sigma$ is ensured. It becomes an approximation as soon as the number of integration point is reduced.

2.4.4 Resolution of the hyper-reduced problem

- *Calculation of the strain-displacement matrix*

The reduced strain-displacement matrix $\hat{\mathbf{B}}$ is obtained from the **B** matrix (which is calculated from the geometry of the elements) and the reduced displacement basis $\boldsymbol{\Phi}_{\mathbf{u}}$ similarly to the equation (35):

$$\underset{(n_{tens}\, x\, n_{PG})\, x\, n_{\hat{\mathbf{u}}}}{\hat{\mathbf{B}}} = \underset{(n_{tens}\, x\, n_{PG})\, x\, n_{\substack{dof \\ total}}}{\mathbf{B}} \; \underset{n_{\substack{dof \\ total}}\, x\, n_{\hat{\mathbf{u}}}}{\boldsymbol{\Phi}_{\mathbf{u}}} \quad (52)$$

As explained before the Gappy Data Reconstruction enables to reduce the analysis to a selection of stress components using the hyper-reduction matrix $\mathbb{A}_\sigma$. Thus the hyper-reduced strain-displacement matrix $\hat{\mathbf{B}}^*$ is given by:

$$\underset{n_{\sigma^* x n_{\hat{u}}}}{\hat{\mathbf{B}}^*} = \underset{n_{\sigma^* x (n_{tens} x n_{PG})}}{\mathbb{A}_{\sigma}^{T}} \underset{(n_{tens} x n_{PG}) x n_{\hat{u}}}{\hat{\mathbf{B}}} \quad (53)$$

In the o*nline part* of the hyper-reduction process the matrix $\mathbf{B}^*$ will denote the matrix composed of the sub-matrices of the reduced matrix $\hat{\mathbf{B}}$ corresponding to the selected components of the stress tensor.

$$\mathbf{B}^* = \begin{bmatrix} \hat{\mathbf{B}}^{(1)} \\ \hat{\mathbf{B}}^{(2)} \\ \vdots \\ \hat{\mathbf{B}}^{(n_{\sigma^*})} \end{bmatrix} \in \mathbb{R}^{n_{\sigma^* x n_{\hat{u}}}} \quad (54)$$

- *Online part*

The input data of the *online part* are the geometrical and material properties, the strain-displacement matrices $\hat{\mathbf{B}}^*$ and $\mathbf{B}^*$, the hyper-reduction matrix $\mathbb{A}_{\sigma}$, the reduced bases and the list of selected stress components and the macroscopic strain imposed to the micro-cell $\boldsymbol{\varepsilon}_{\text{macro}}$.

The computation of the reduced internal force vector $\hat{\mathbf{f}}^{\text{int}}$ is performed similarly to the equation (37):

$$\left\{\hat{\mathbf{f}}^{\text{int}}\right\}^e = \int_{V^e} \left[\hat{\mathbf{B}}^e\right]^T \cdot \boldsymbol{\sigma}^e \, dV \cong \sum_{i_{PG}=1}^{n_{PG}} w^{(i_{PG})} \left[\hat{\mathbf{B}}^e_{i_{PG}}\right]^T \cdot \boldsymbol{\sigma}^e_{i_{PG}} \cdot |\, \mathbf{J}^e_{i_{PG}} \,| \cdot V^e \quad (55)$$

$$\underset{n_{\hat{u}} x 1}{\hat{\mathbf{f}}^{\text{int}}} = \hat{\mathbf{B}}^T \mathbb{S} = \hat{\mathbf{B}}^T \mathbb{A}_{\sigma} \mathbb{S}^* = \underset{n_{\hat{u}} x n_{\sigma^*}}{\left[\hat{\mathbf{B}}^*\right]^T} \underset{n_{\sigma^* x 1}}{\mathbb{S}^*} \quad (56)$$

The stress $\mathbb{S}^*$ is linked to the reduced displacement $\hat{\mathbf{u}}$ by the reduced consistent tangent operator $\mathbb{C}^*$.

$$\underset{n_{\sigma^* x 1}}{\mathbb{S}^*} = \underset{n_{\sigma^* x n_{\sigma^*}}}{\mathbb{C}^*} \underset{n_{\sigma^* x n_{\hat{u}}}}{\mathbf{B}^*} \underset{n_{\hat{u}} x 1}{\hat{\mathbf{u}}} \quad (57)$$

This reduced consistent tangent operator $\mathbb{C}^*$ is composed, on the diagonal, of the sub-matrices of the full consistent tangent operator corresponding to the selected stress components.

$$\mathbb{C}^* = \begin{bmatrix} \mathbf{C}^{(1)} & & & \\ & \mathbf{C}^{(2)} & & (0) \\ & & \mathbf{C}^{(3)} & \\ & (0) & & \ddots \\ & & & & \mathbf{C}^{(n_{\sigma^*})} \end{bmatrix} \in \mathbb{R}^{n_{\sigma^*} x n_{\sigma^*}} \qquad \textbf{(58)}$$

Thus the expression (56) becomes:

$$\hat{\mathbf{f}}^{\text{int}} = \left[\hat{\mathbf{B}}^*\right]^T \mathbb{C}^* \mathbf{B}^* \hat{\mathbf{u}} = \hat{\mathbf{K}}^* \hat{\mathbf{u}} \qquad \textbf{(59)}$$

where the stiffness matrix $\hat{\mathbf{K}}^*$ is given by:

$$\underset{n_{\hat{\mathbf{u}}} x n_{\hat{\mathbf{u}}}}{\hat{\mathbf{K}}^*} = \underset{n_{\hat{\mathbf{u}}} x n_{\sigma^*}}{\left[\hat{\mathbf{B}}^*\right]^T} \underset{n_{\sigma^*} x n_{\sigma^*}}{\mathbb{C}^*} \underset{n_{\sigma^*} x n_{\hat{\mathbf{u}}}}{\mathbf{B}^*} \qquad \textbf{(60)}$$

The hyper-reduction problem is now posed. As in the first reduced models it is numerically solved using the iterative Newton-Raphson algorithm.

For each iteration *k* the new reduced displacement guess is computed adding an increment $\Delta\hat{\mathbf{u}}^{k+1}$ to the previous guess $\hat{\mathbf{u}}^k$.

$$\hat{\mathbf{u}}^{k+1} = \hat{\mathbf{u}}^k + \Delta\hat{\mathbf{u}}^{k+1} \qquad \textbf{(61)}$$

where

$$\underset{n_{\hat{\mathbf{u}}} x 1}{\Delta\hat{\mathbf{u}}^{k+1}} = -\underbrace{\left[\hat{\mathbf{K}}^{*\,k}\right]}_{n_{\hat{\mathbf{u}}} x n_{\hat{\mathbf{u}}}}^{-1} . \underbrace{\left[\hat{\mathbf{res}}^k\right]}_{n_{\hat{\mathbf{u}}} x 1} \qquad \textbf{(62)}$$

and

$$\underbrace{\left[\hat{\mathbf{res}}^k\right]}_{n_{\hat{\mathbf{u}}} x 1} = \underset{n_{\hat{\mathbf{u}}} x 1}{\hat{\mathbf{f}}^{\text{int}}} - \underset{n_{\hat{\mathbf{u}}} x 1}{\hat{\mathbf{f}}^{ext}} \qquad \textbf{(63)}$$

The accuracy of this hyper-reduced model is determined by the "quality" of the snapshot matrices, the choice of the dimensions of the truncated bases $n_{\hat{\mathbf{u}}}$ and n_{σ} , the number n_{σ^*} of selected stress components for the Gappy Data Reconstruction and the selection strategy of these components.

- *Relationship between* $n_{\hat{u}}$, n_{σ} *and* n_{σ^*}

To avoid singularities it is important to respect some relationships between the dimensions $n_{\hat{u}}$, n_{σ} and n_{σ^*} .

Firstly, the equation $\underset{n_{\boldsymbol{\sigma}} x1}{\hat{\boldsymbol{\varepsilon}}} = \underset{n_{\boldsymbol{\sigma}} x n_{\hat{\mathbf{u}}}}{\hat{\mathbf{B}}} \; \underset{n_{\hat{\mathbf{u}}} x1}{\hat{\mathbf{u}}} = 0$ must only have the trivial solution $\hat{\mathbf{u}} = 0$.

Thus to avoid the reduced strain-displacement matrix $\hat{\mathbf{B}}$ to be singular the dimension of the truncated displacement basis has to be inferior to the one of the truncated stress basis.

$$n_{\hat{u}} \leq n_{\sigma} \tag{64}$$

Furthermore the hyper-reduced stress vector $\boldsymbol{\sigma}^*$ is computed from the reduced stress vector by the relationship:

$$\underset{n_{\boldsymbol{\sigma}^*} x1}{\boldsymbol{\sigma}^*} = \underset{n_{\boldsymbol{\sigma}^*} x n_{\boldsymbol{\sigma}}}{\boldsymbol{\Phi}^*} \; \underset{n_{\boldsymbol{\sigma}} x1}{\hat{\boldsymbol{\sigma}}} \tag{65}$$

Thus the matrix $\boldsymbol{\Phi}^*$ also has to be no singular which implies that the number of selected stress component has to be greater than the dimension of the truncated stress basis.

$$n_{\sigma} \leq n_{\sigma^*} \tag{66}$$

Finally, these three parameters have to respect the following relationship:

$$n_{\hat{u}} \leq n_{\sigma} \leq n_{\sigma^*} \tag{67}$$

The numerical examples presented in the chapter 3 developed the effect of these dimensions on the convergence and the accuracy of the computational solution.

2.4.5 Synthesis of the hyper-reduction of the micro-scale problem

The hyper-reduction process can be split into two distinct parts: the *offline part* which contains the preparation steps of the micro-scale problem and the *online part* which is run for the resolution of the multi-scale problem to determine the constitutive equation of each Gauss point of the macroscopic mesh.

- *Offline part*

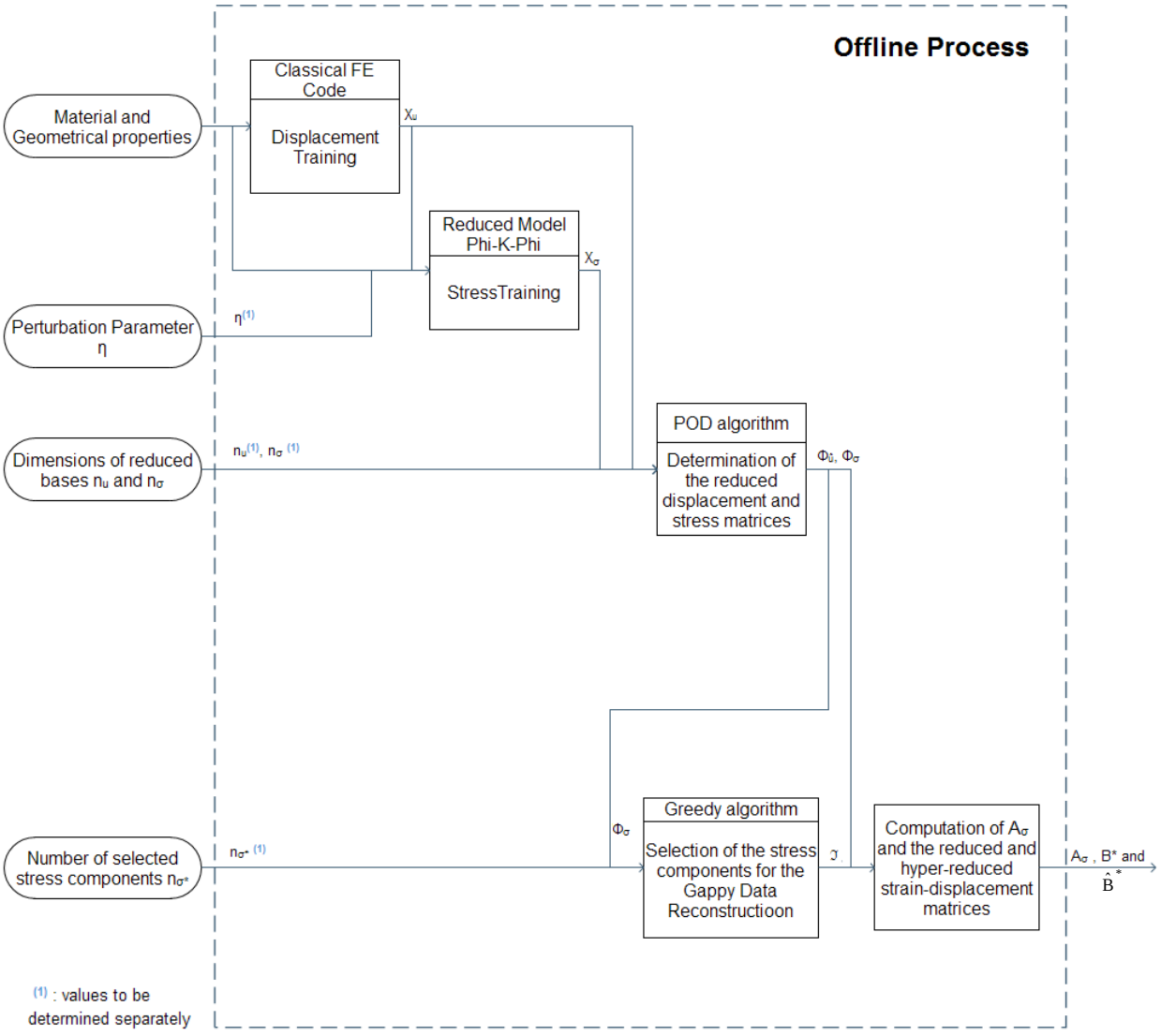

Figure 2.4 : Diagram of the offline process of the hyper-reduction

- *Online part*

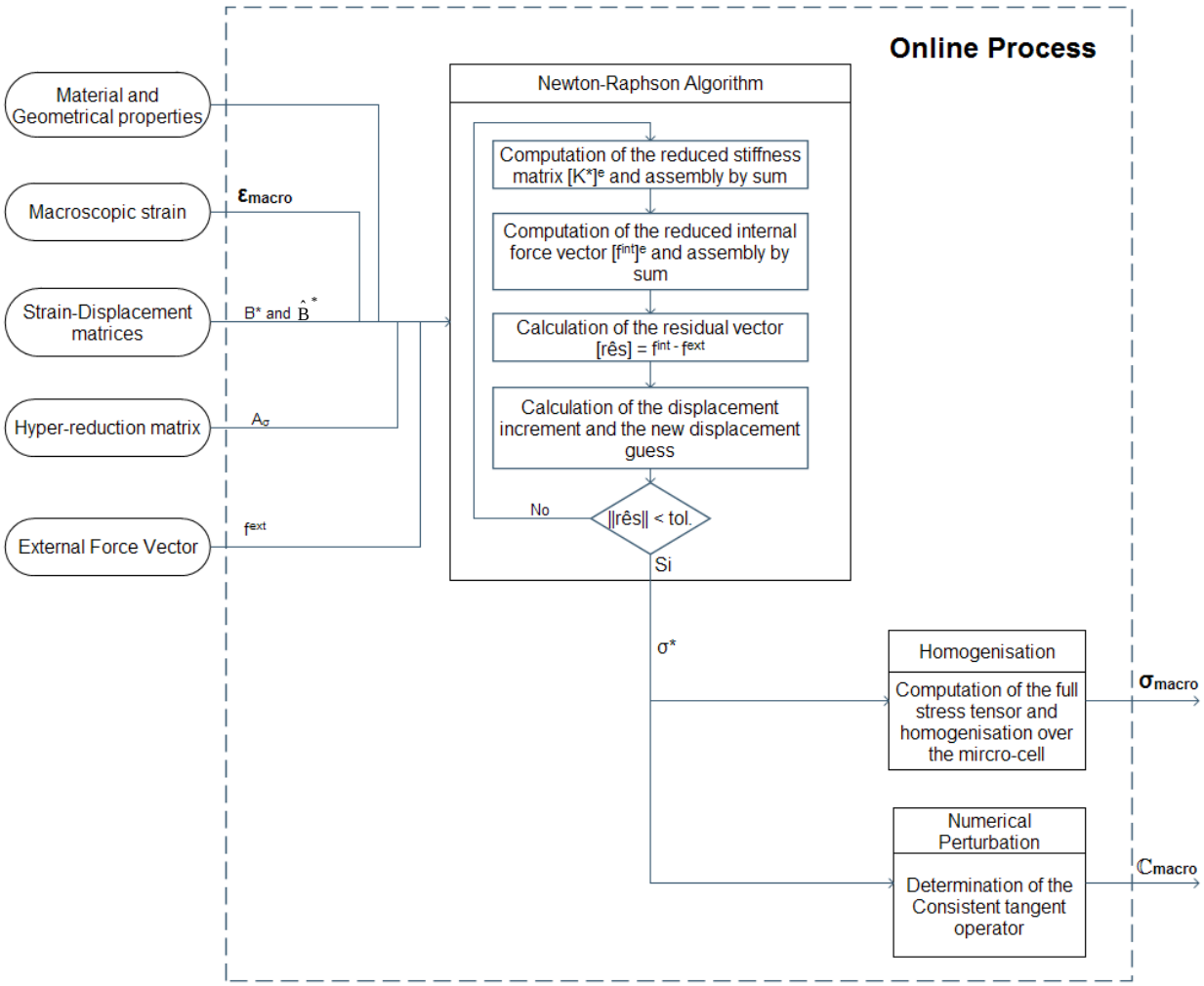

Figure 2.5 : Diagram of the online process of the hyper-reduction

Chapter 3:

Numerical Examples

The *Chapter 3* presents the results of the reduction and hyper-reduction models implemented. It is split into 2 parts. The first one provides an analysis on the micro-scale problem. In the second one, 2 complete multi-scale problems are studied. The model named High Fidelity (HF) refers to the classical Finite Element approach without using model order reduction techniques.

3.1 Analysis on the micro-scale problem

3.1.1 Efficiency of the model order reduction techniques on the micro-cell

The example treated in this paragraph is the case of a clamped square Representative Volume Element with a hole at the centre. Three meshes are used with various degrees of discretization around the hole. They are presented in the *Figure 3.1*.

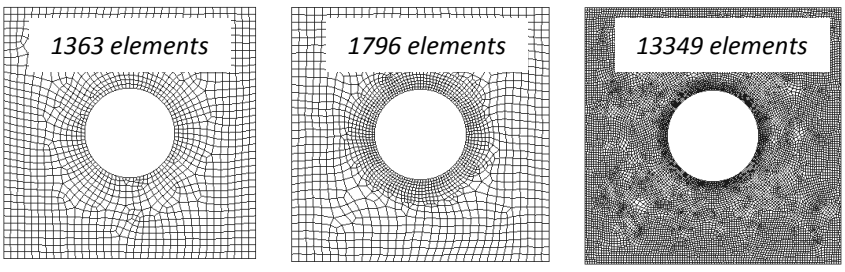

Figure 3.1 : Meshes used to analyze the efficiency of the model order reduction

- *Plasticity model*

The first model implemented is a plane J2 plasticity model with isotropic hardening. The values of the material parameters are:

Young Modulus	:	E = 2.1 GPa
Poisson ratio	:	$\nu = 0.3$
Initial yield stress	:	$\sigma_y = 1000$ MPa
Kinematic hardening parameter	:	H = 0.0

The generation of the displacement snapshot matrix uses a training strain path in the direction ε_x, ε_y and γ_{xy} and contains an elastic part and a plastic part.

The *Figure 3.2*, *Figure 3.3* and *Figure 3.4* present the evolution of the homogenized stress-strain graphic according to the model order reduction technique and the number of displacement snapshots used.

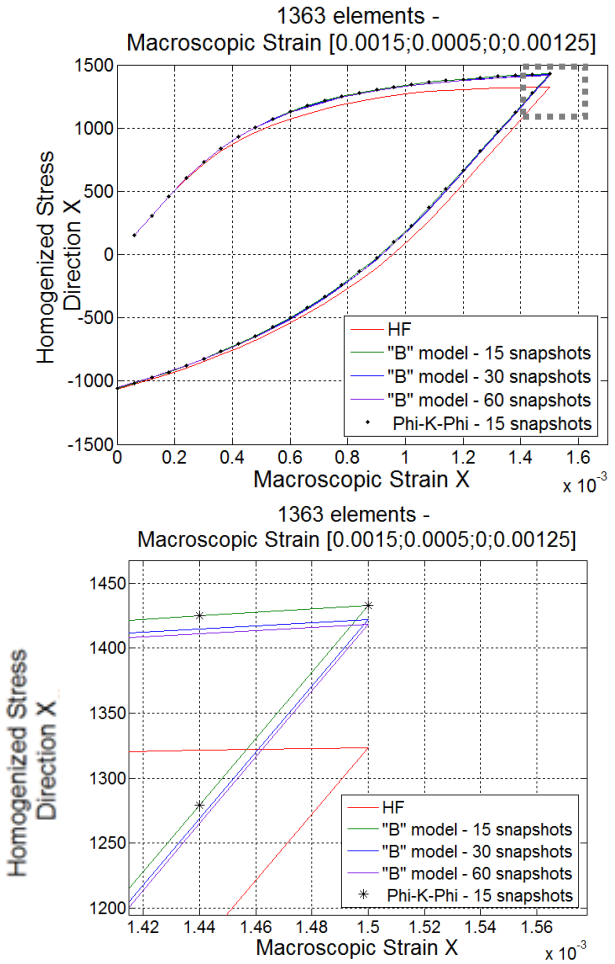

Figure 3.2 : Stress-strain graphic in direction X for J2 plasticity model

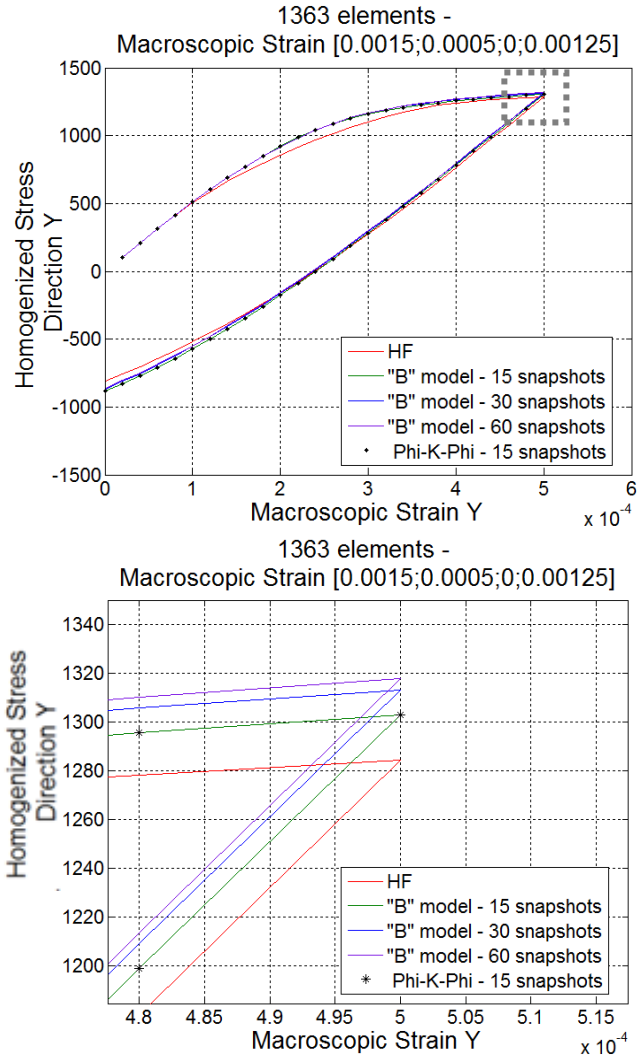

Figure 3.3 : Stress-strain graphic in direction Y for J2 plasticity model

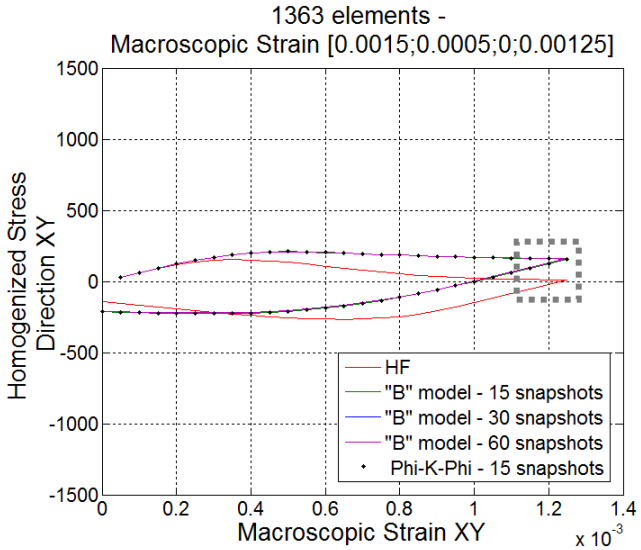

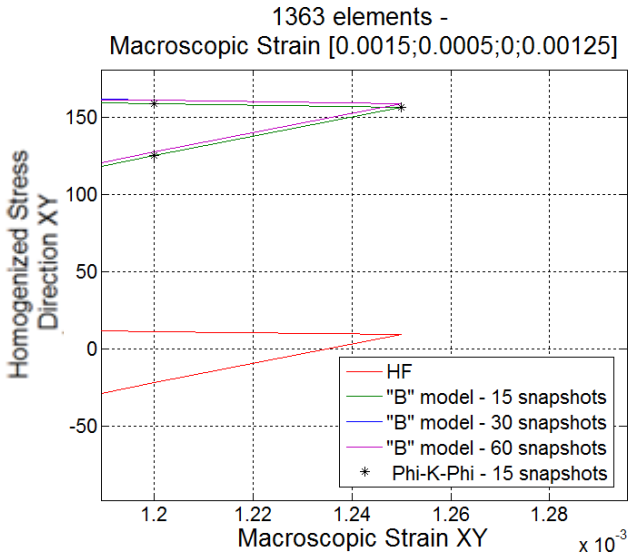

Figure 3.4 : Stress-strain graphic in direction XY for J2 plasticity model

In all directions the reduced models "Phi-K-Phi" and "$\hat{B}$" provide exactly the same results. Thus the calculation or not of the full stiffness matrix before working with the reduced stiffness matrix, which is the main difference between these two models, does not change the final results.

Furthermore it seems that the number of displacement snapshots used during the training phase does not affect significantly the accuracy. Thus fifteen displacement snapshots (i.e. six in each direction) are sufficient to approach the exact solution.

Besides it appears that the stresses in the direction X and Y are well captured by these reduced models while the difference between the classical Finite Element model (HF) and the reduced models is more important in the direction XY than in the two other directions, especially in the plastic part of the path. Even increasing the number of displacement snapshots in this particular direction does not make it possible to increase the accuracy. Nevertheless these accuracy results are globally satisfactory.

The *Table 3.1* presents the speed up results obtained with the two reduced models implemented. The "$\hat{B}$" model enables to reach a slightly higher speed up than the "Phi-K-Phi" model. However these two methods do not make it possible to achieve a speed up higher than 1.37 whatever the degree of discretization of the mesh.

# elements	# displacement snapshots	# displacement modes used $n_{\hat{u}}$	"Phi-K-Phi" Speed Up	" $\hat{B}$ " model Speed Up
1 363	15	12	**1.10**	**1.18**
1 796	15	13	**1.16**	**1.30**
13 349	15	13	**1.24**	**1.37**

Table 3.1: Speed up results for the J2 plasticity model

In what follows the analysis uses a damage model.

- *Damage model*

A damage model with a pseudo-hardening behaviour is analyzed and uses the following material parameters:

Young Modulus	:	E = 2.1 GPa
Poisson ratio	:	$\nu = 0.3$
Initial yield stress	:	σ_y = 1000 MPa

The results for three values of the pseudo-hardening parameter are analyzed: H=0.5, H=0.333 and H=0.05.

The *Figure 3.5*, *Figure 3.6* and *Figure 3.7* present the homogenized stress-strain graphics in the three directions respectively for H=0.5, H=0.333 and H=0.05 in the case of the 1363-element mesh. As noted before the "Phi-K-Phi" reduced model and the " $\hat{B}$ " reduced model give exactly the same results. Thus only the results of the " $\hat{B}$ " model are presented in these figures.

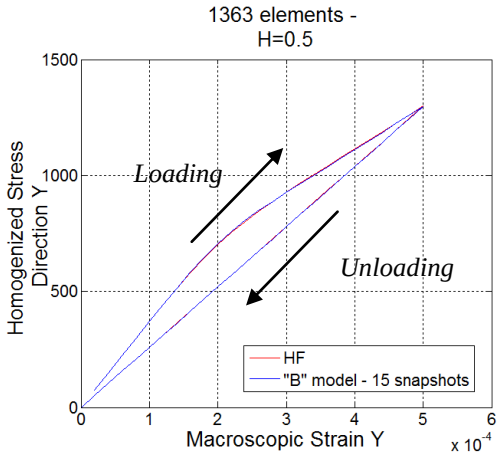

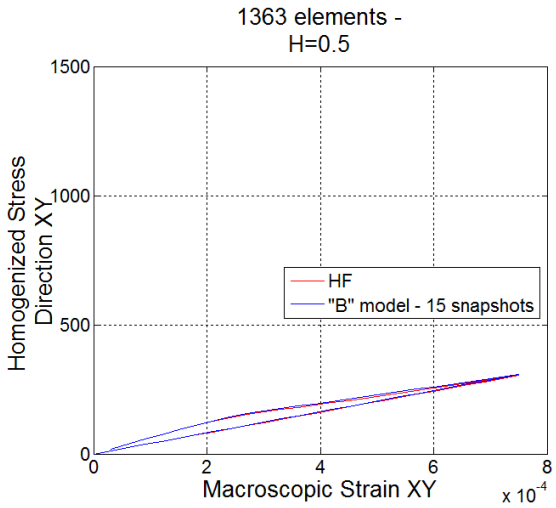

Figure 3.5 : Stress-strain graphics for damage model with H=0.5

For a high value of the pseudo-hardening parameter H, the *Figure 3.5* shows that the reduced models provide an approximation nearly exact.

Decreasing this value until 0.333 small errors start appearing as shown in the *Figure 3.6*. The speed up achieved, presented in the *Table 3.2*, is similar to the one obtain with the plasticity model, around 1.20.

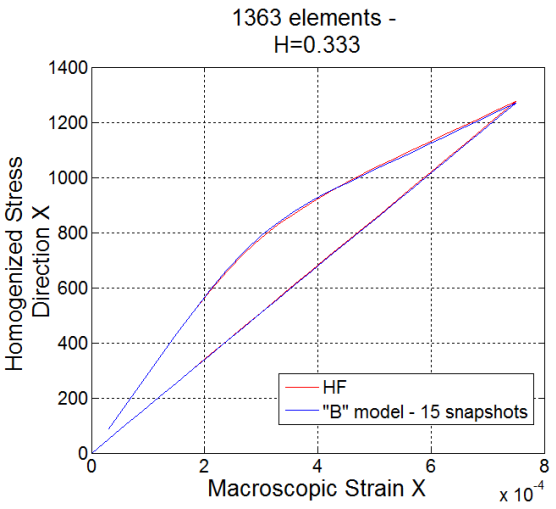

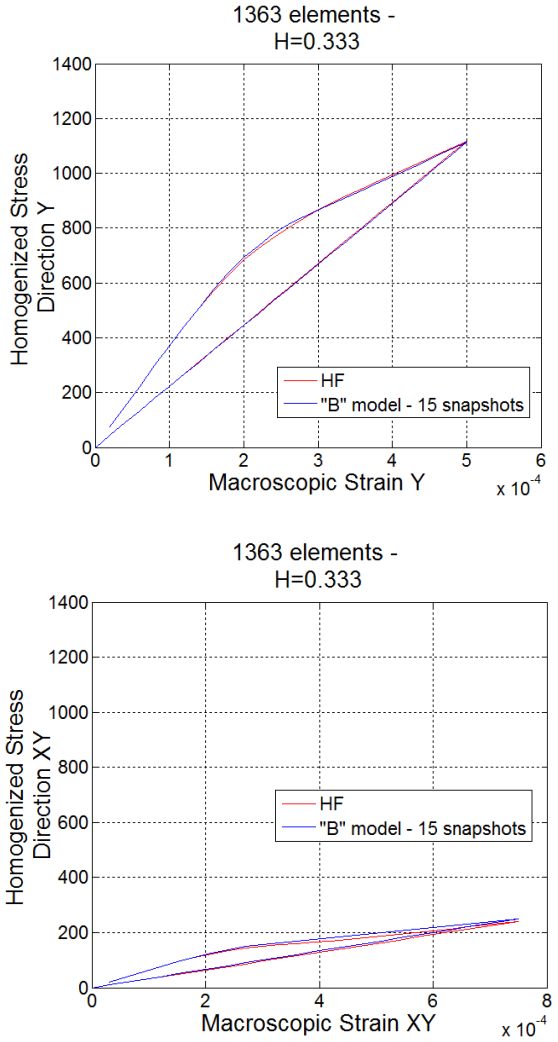

Figure 3.6 : Stress-strain graphics for damage model with H=0.333

# elements	# displacement snapshots	# displacement modes used $n_{\hat{u}}$	"Phi-K-Phi" Speed Up	"$\hat{\mathbf{B}}$" model Speed Up
1 363	15	10	**1.16**	**1.27**
1 796	15	10	**1.17**	**1.29**

Table 3.2: Speed up results for damage model with H=0.333

In the case of H=0.05 the reduced models have more difficulties to approximate the damage part of the curve while the elastic part and the unload part are exactly estimated. The error is particularly more important in the direction XY as shown in the *Figure 3.7*. Regarding the speed up results presented in the *Table 3.3* they are higher than for higher values of the pseudo-hardening parameter H, but stays relatively low.

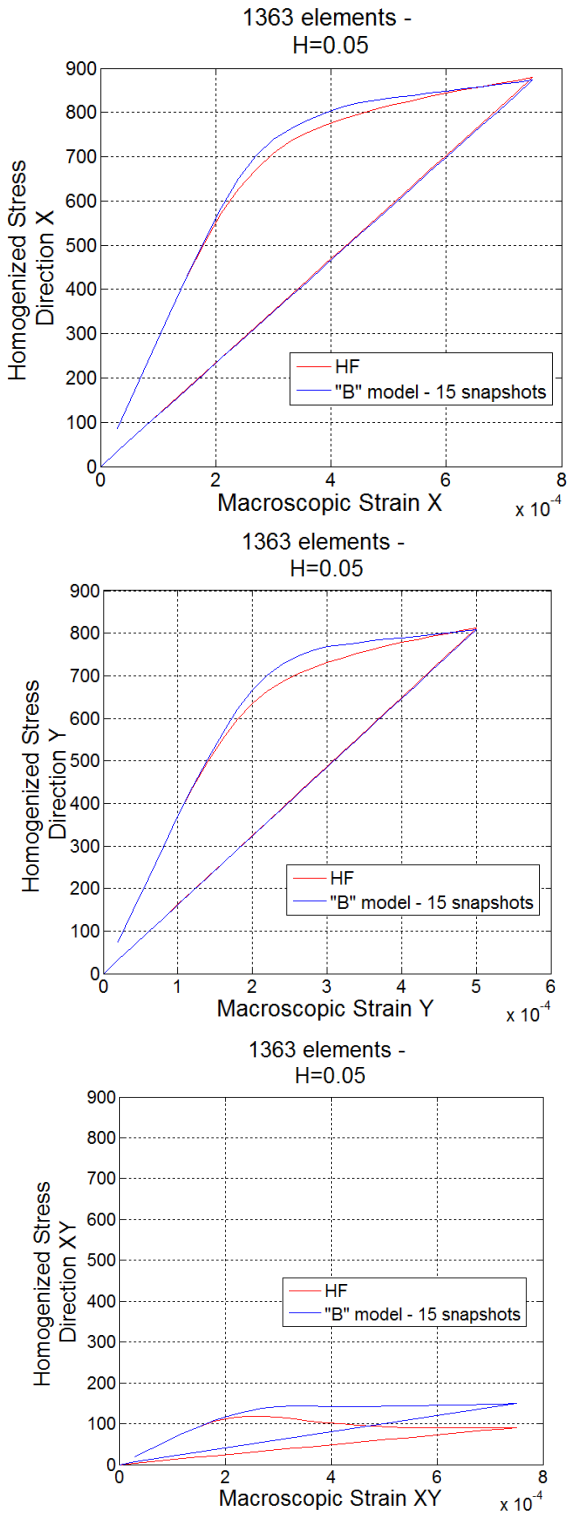

Figure 3.7 : Stress-strain graphics for damage model with H=0.05

# elements	# displacement snapshots	# displacement modes used $n_{\hat{u}}$	"Phi-K-Phi" Speed Up	"$\hat{\mathbf{B}}$" model Speed Up
1 363	15	10	**1.28**	**1.47**
1 796	15	10	**1.33**	**1.49**

Table 3.3: Speed up results for damage model with H=0.05

The speed up achieved with the "Phi-K-Phi" reduced model as well as the "$\hat{\mathbf{B}}$" reduced model are disappointing that is why a hyper-reduction of the micro-scale problem is then tested.

3.1.2 Efficiency of the hyper-reduction procedure on the micro-cell

A damage model similar to the one analyzed in the previous paragraph is used with a kinematic hardening parameter H equal to 0.1.

- *One-hole square example*

The first part of this paragraph uses the case of the same clamped square micro-cell with a hole at the centre. The mesh is slightly coarser; it is now composed of 1024 elements.

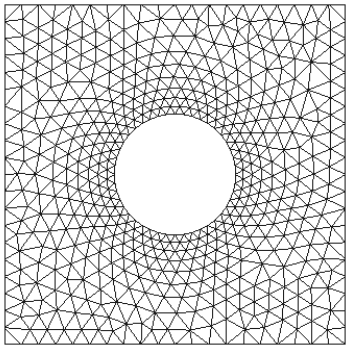

1024 elements

Figure 3.8 : Mesh of the one-hole square used to test the hyper-reduction method

Regarding the displacement and stress snapshot matrices, each one contains 18 snapshots. Thus the maximum number of displacement or stress modes available is 18.

➔ *Interest of the perturbation force in the generation of the stress snapshot matrix*

As explains in the paragraph 2.4.1 the generation of the stress snapshot matrix uses a perturbation force which depends on the parameter η. The *Table 3.4* shows the interest of this perturbation. Indeed when the parameter η is not null the cases of divergence of the Newton-Raphson algorithm are less frequent than in absence of perturbation. Moreover increasing the number n_σ of stress modes the convergence is only lost when the equation (66) is not respect, i.e. when n_σ becomes higher than the number of stress components selected verified $n_{\sigma*} = n_{elem*} \times n_{tens} = 3n_{elem*}$. When $\eta \neq 0$ the speed up is lightly inferior but the method seems more stable as the number of stress modes increases.

It can be notice that the speed up achieved using the hyper-reduction technique is around 200 which is considerably higher than the ones obtained before which were around 1.2.

# displacement modes used $n_{\hat{u}}$	**# stress modes used** n_σ	**# elements selected** n_{elem*}	**η**	**Speed Up**	**Displacement Error**	**Stress Error**
5	**7**	5	**0**	**292.6**	13,91%	12,67%
5	**8**	5	**0**	**307.2**	44,64%	27,62%
5	**9**	5	**0**		Not converged	
5	**10**	5	**0**	**287.6**	0,50%	1,02%
5	**11**	5	**0**		Not converged	
5	**12**	5	**0**	**275.9**	0,63%	3,21%
5	**13**	5	**0**	**266.8**	1,96%	13,54%
5	**14**	5	**0**		Not converged	
5	**15**	5	**0**		Not converged	
5	**7**	5	**100**		Not converged	
5	**8**	5	**100**		88,1%	118,8%
5	**9**	5	**100**	**176.7**	4,94%	11,32%
5	**10**	5	**100**	**208.0**	0,08%	3,11%
5	**11**	5	**100**	**206.1**	0,08%	3,11%
5	**12**	5	**100**	**223.4**	0,08%	3,05%
5	**13**	5	**100**	**211.8**	0,09%	3,10%
5	**14**	5	**100**	**198.3**	0,09%	3,13%
5	**15**	5	**100**	**203.9**	0,09%	3,13%

Table 3.4: Analysis of the effect of the perturbation force in the stress snapshot matrix generation on the hyper-reduction results

The displacement and stress errors presented in the *Table 3.4* and in all that follows are calculated from the results of the High Fidelity models $\mathbf{u}^{HF}$ and $\boldsymbol{\sigma}^{HF}$:

$$Displacement\ Error = \frac{\int_\Omega \left|\mathbf{u} - \mathbf{u}^{HF}\right|^2 \mathrm{dV}}{\int_\Omega |\mathbf{u}|^2 \mathrm{dV}} \quad \textbf{(68)}$$

$$Stress\ Error = \frac{\int_\Omega \left|\boldsymbol{\sigma} - \boldsymbol{\sigma}^{HF}\right|^2 \mathrm{dV}}{\int_\Omega |\boldsymbol{\sigma}|^2 \mathrm{dV}} \quad \textbf{(69)}$$

➔ *Stress component selection strategies*

In the previous tests the stress component selection for the Gappy Data Reconstruction has been performed using the Greedy algorithm. But as presented in the paragraph 2.4.2 a POD reconstruction-based algorithm can also been implemented.

The *Table 3.5* presents the accuracy results of these two methods obtained for various numbers of stress modes and selected elements. The displacement error computed is generally inferior when the POD reconstruction-based algorithm is used but on the other hand the stress error is slightly higher.

Regarding the occurrence of divergence cases as the number of elements selected increases there is no clear tendency. Indeed for $n_\sigma = 6$ or $n_\sigma = 10$ the convergence is not lost by increasing n_{elem^*} in the POD reconstruction-based case contrary to the results of the Greedy algorithm. But for $n_\sigma = 9$ divergence cases appear for $n_{elem^*} = 5, 6$ or 8 while accurate results have been obtained with 4 elements.

Thus no one of these two stress components selection strategies can totally ensure the convergence of the Newton-Raphson algorithm. Nevertheless the Greedy algorithm will be used in what follows.

$n_{\hat{u}}$	n_σ	n_{elem*}	**Greedy algorithm**		**POD reconstruction-based algorithm**	
			Displacement error	Stress error	Displacement error	Stress error
4	**6**	5	7.81%	2.77%	Not converged	
4	**6**	6	7.17%	2.22%	Not converged	
4	**6**	7	35.72%	8.31%	0.33%	6.66%
4	**6**	10	13.08%	2.25%	0.33%	6.68%
4	**6**	11	Not converged		1.28%	2.57%
4	**6**	12	Not converged		0.77%	2.74%
4	**6**	13	14.60%	4.28%	0.94%	2.72%
4	**6**	17	8.33%	4.17%	0.35%	3.66%
4	**7**	5	7.19%	6.33%	Not converged	
4	**7**	6	45.57%	9.27%	0.20%	7.81%
4	**7**	7	4.51%	2.30%	0.21%	7.78%
4	**7**	8	6.64%	2.68%	0.21%	7.76%
4	**7**	10	6.50%	2.95%	0.23%	6.20%
4	**7**	11	4.63%	3.30%	0.18%	6.28%
4	**7**	13	4.39%	2.77%	0.19%	6.23%
4	**7**	15	3.56%	2.78%	0.19%	6.13%
4	**7**	17	4.34%	2.49%	0.20%	7.35%
4	**9**	4	0.12%	1.39%	0.60%	2.09%
4	**9**	5	0.19%	0.74%	Not converged	
4	**9**	6	0.23%	0.70%	Not converged	
4	**9**	7	0.32%	0.72%	161.74%	42.15%
4	**9**	8	0.21%	0.73%	Not converged	
4	**9**	10	0.16%	0.76%	0.14%	0.92%
4	**9**	11	0.13%	0.75%	0.20%	1.05%
4	**9**	12	Not converged		0.08%	0.95%
4	**9**	15	Not converged		0.17%	0.90%
4	**9**	17	Not converged		Not converged	
4	**10**	4	0.14%	1.53%	Not converged	
4	**10**	5	Not converged		0.33%	2.63%
4	**10**	6	Not converged		0.06%	1.13%
4	**10**	8	Not converged		0.07%	1.15%
4	**10**	9	0.25%	0.84%	0.07%	1.14%
4	**10**	10	0.26%	0.85%	0.07%	1.13%
4	**10**	17	0.11%	0.80%	0.06%	1.24%

Table 3.5: Comparison of the accuracy results of the Greedy algorithm and the POD reconstruction-based algorithm

- *Asymmetric two-hole square example*

The second part of this paragraph studies the case of a clamped asymmetric two-hole square micro-cell. The mesh contains 1639 elements and is presented in the *Figure 3.9*.

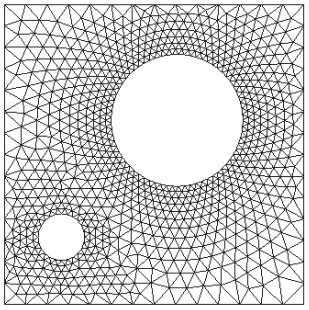

Figure 3.9 : Mesh of the asymmetric two-hole square used to test the hyper-reduction method

42 displacement and stress snapshots are generated in the *offline part* of the process.

The *Table 3.6* presents the speed up and accuracy results of the hyper-reduction method for two different values of the parameter η and various dimensions n_σ of the reduced stress basis.

$n_{\hat{u}}$	n_σ	n_{elem*}	η	**Speed Up**	**Displacement Error**	**Stress Error**
4	**5**	4	**1000**	**456.9**	0.79%	10.72%
4	**6**	4	**1000**	**466.7**	0.39%	9.66%
4	**7**	4	**1000**	**437.0**	1.89%	21.00%
4	**8**	4	**1000**		Not converged	
4	**9**	4	**1000**		Not converged	
4	**10**	4	**1000**		Not converged	
4	**11**	4	**1000**		Not converged	
4	**12**	4	**1000**	**322.2**	1.12%	33.39%
4	**5**	4	**50**	**460.6**	0.90%	7.90%
4	**6**	4	**50**	**437.2**	0.44%	6.18%
4	**7**	4	**50**	**462.3**	0.21%	5.97%
4	**8**	4	**50**	**440.2**	0.38%	7.12%
4	**9**	4	**50**	**396.8**	0.92%	26.04%
4	**10**	4	**50**	**419.1**	0.58%	10.64%
4	**11**	4	**50**	**447.8**	0.76%	6.87%
4	**12**	4	**50**	**380.2**	0.59%	7.04%

Table 3.6: Analysis of the hyper-reduction results on the asymmetric two-hole square problem

For η = 1000 divergence cases are more frequent than for a smaller value of this parameter. Moreover the errors computed are lower and the speed up slightly higher for η = 50. Thus it seems that as η decreases the solution of the hyper-reduction process is more stable and closer to the classical Finite Element solution. Nevertheless when the value of the parameter η becomes too small (η < 50 for this problem and η < 30 for the one-hole problem) a lot of divergence cases appear.

Thus the value of η has to be chosen as small as possible to generate a stress snapshot matrix close enough to the equilibrium curve but not exactly on it to avoid singularity.

Regarding the relationship between the dimensions $n_{\hat{u}}$, n_{σ} and n_{σ^*} , in addition to the respect of the equation (67), it has been observed in the two problems studied in this hyper-reduction paragraph that a good compromise between stability, accuracy and speed up is generally obtained for $n_{\sigma} = n_{\hat{u}} + n_{elem^*}$ and $n_{elem^*} = n_{\hat{u}}$ where n_{elem^*} is defined as $n_{elem^*} = \frac{n_{\sigma^*}}{n_{tens}} = \frac{n_{\sigma^*}}{3}$. Moreover a judicious value for the dimension $n_{\hat{u}}$ of the reduced displacement basis seems to be half of the rank of the displacement snapshot matrix. These relationships are experimental observations and have not been justified analytically.

3.2 Examples of multi-scale problems

The hyper-reduction process of the micro-scale problem is now introduced in the resolution of a global multi-scale problem. In what follows the micro-structure considered is a one-hole square micro-cell presented in the *Figure 3.8*.

During the training of the micro-cell 18 displacement and stress snapshots have been generated, using a perturbation parameter η equal to 30 in the stress training. As long as the number of elements n_{elem^*} used for the Gappy Data Reconstruction is inferior to this number of snapshots the stress components selection can be performed by the Greedy algorithm. But it is not possible to select more elements with this algorithm because the addition of one element is based on the reconstruction of one mode as detailed in the

paragraph 2.4.2. Thus only the selections of less than 18 elements are performed by the Greedy algorithm in what follows.

3.2.1 Simple square

The first multi-scale problem analyzed is the case of a simple square split into 2 triangular elements. The geometry and the macroscopic boundary conditions are presented in the *Figure 3.10*.

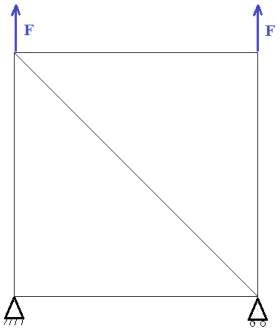

Figure 3.10 : Mesh of the simple square multi-scale example

The *Table 3.7* presents the speed up and accuracy results for the resolution of this multi-scale problem for various combinations of hyper-reduction parameters. As the number of elements used during the hyper-reduction increases the speed up decreases. Nevertheless a good accuracy can be achieved with a speed up of almost 100. While the displacement error varies between 23% and 5% the evaluation of the stress tensor is almost exact.

$n_{\hat{u}}$	n_σ	n_{elem^*}	**Speed up**	**Displacement Error**	**Stress Error**
4	8	**4**	**111.2**	23.56%	10.9e-9 %
4	8	**5**	**88.7**	18.24%	5.9e-9 %
4	8	**6**	**91.9**	15.84%	1.1e-9 %
4	8	**8**	**83.5**	8.00%	1.0e-9 %
4	8	**10**	**75.5**	9.07%	7.8e-9 %
4	8	**15**	**49.2**	12.83%	3.7e-9 %
4	10	**25**	**53.2**	8.04%	1.1e-8 %
4	10	**50**	**28.1**	6.31%	6.6e-9 %
4	10	**100**	**15.9**	5.53%	1.4e-9 %
4	10	**200**	**7.8**	5.22%	1.3e-9 %
4	10	**500**	**3.4**	5.12%	1.9e-9 %

Table 3.7: Results of the multi-scale problem of the simple square

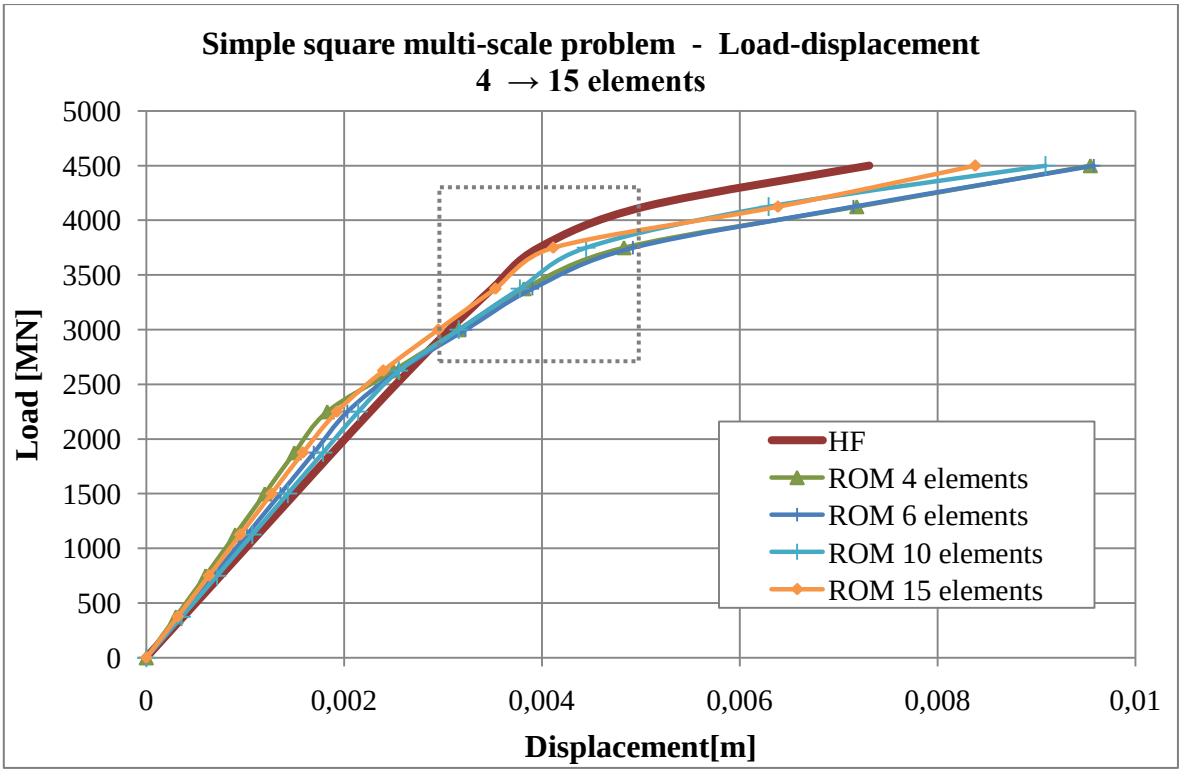

Figure 3.11 : Load-displacement graphics for the resolution of the simple square multi-scale example using 4 to 15 elements

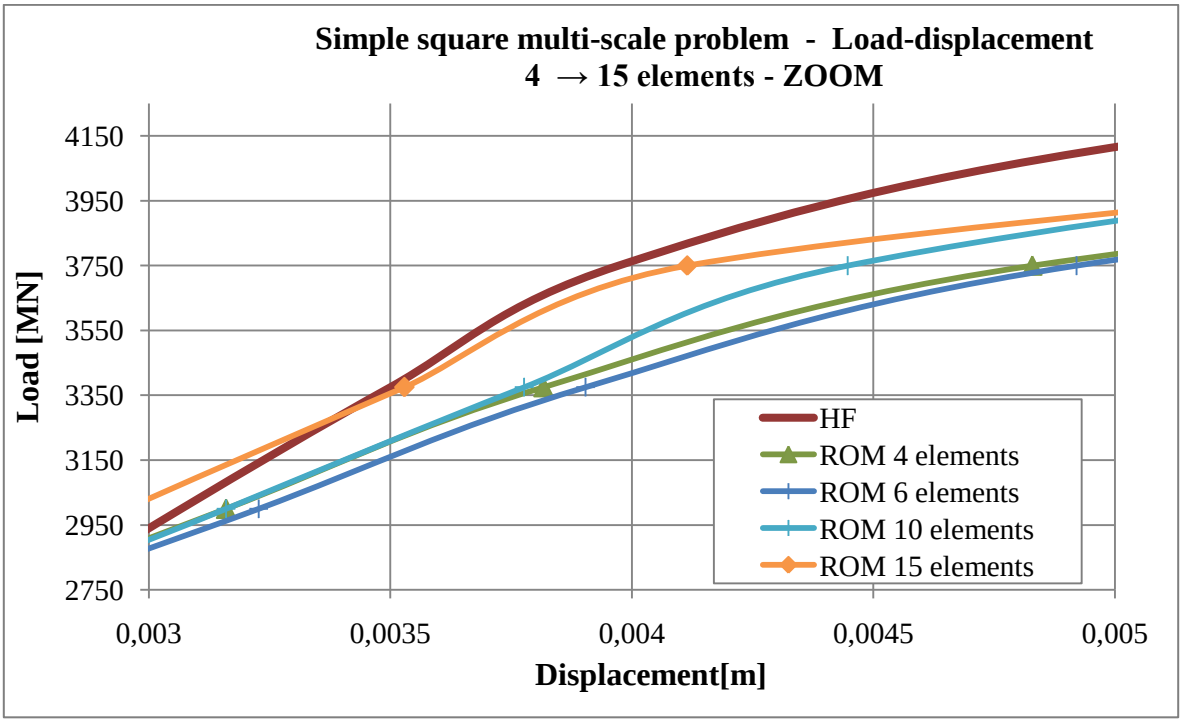

Figure 3.12 : Load-displacement graphics for the resolution of the simple square multi-scale example using 4 to 15 elements - Zoom

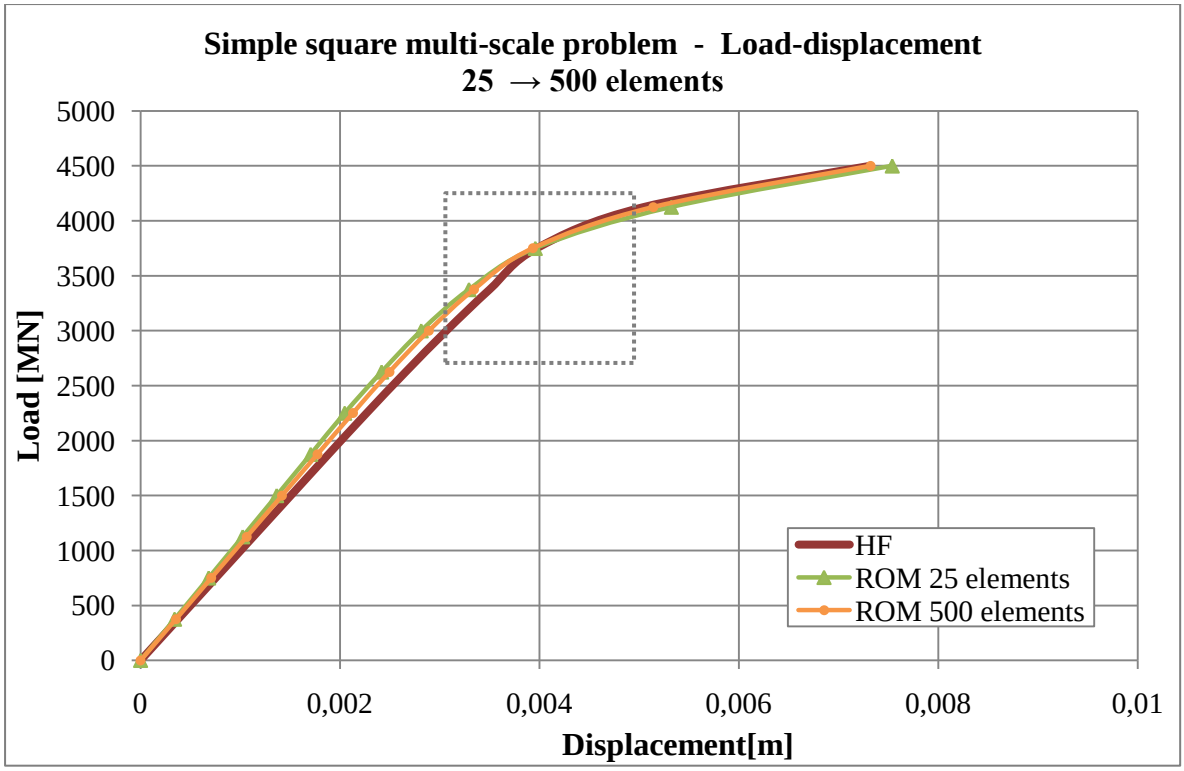

Figure 3.13 : Load-displacement graphics for the resolution of the simple square multi-scale example using 25 to 500 elements

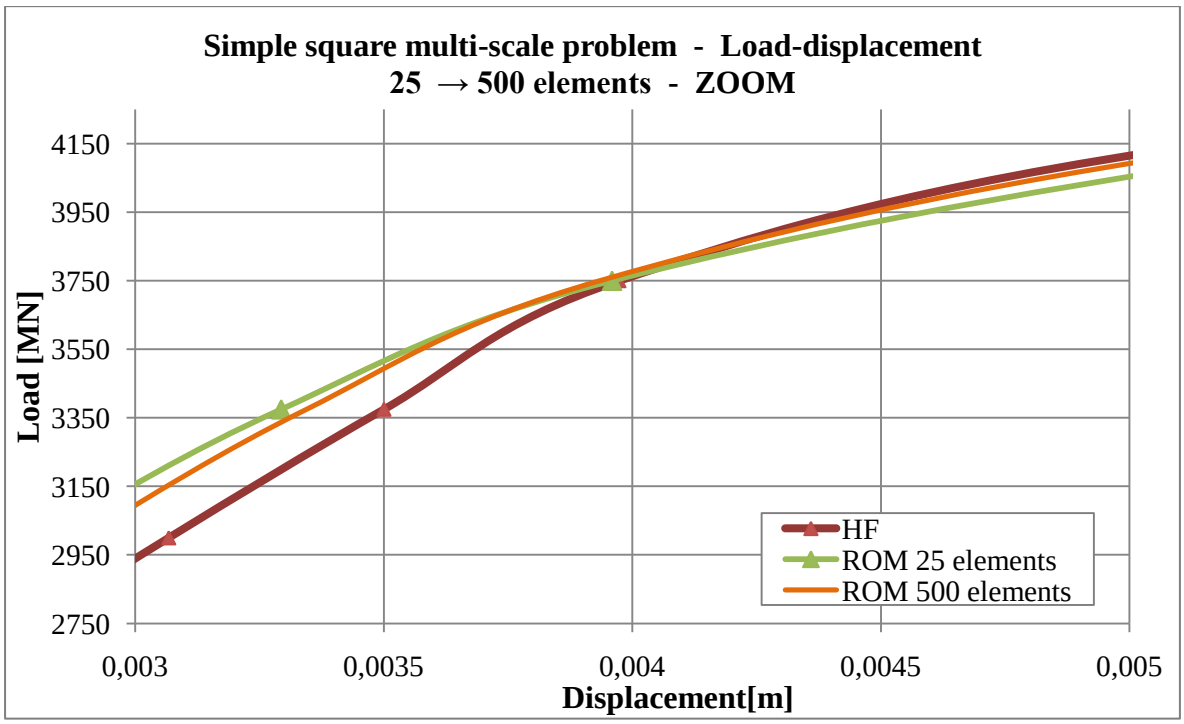

Figure 3.14 : Load-displacement graphics for the resolution of the simple square multi-scale example using 25 to 500 elements – Zoom

The *Figure 3.11* and *Figure 3.12* enable to compare the macroscopic load-displacement graphics obtained using 4, 6, 10 and 15 elements in the hyper-reduction process of the micro-scale problem. The results for 25 to 500 elements used in the Gappy Data Reconstruction are presented in the *Figure 3.13* and *Figure 3.14*. The notation HF refers to the classical Finite Element model and ROM to the multi-scale algorithm using the hyper-reduction procedure to solve the micro-scale problem.

This procedure seems consistent; indeed as the number of elements used tends to the total number of element of the micro-cell the results tend to the exact response. But the utilization of 4 elements already ensures accurate results with an efficient decrease of the computational cost.

This resolution of this simple multi-scale problem enables us to verify the performance of the algorithm before dealing with a more complicated mesh in the next paragraph.

3.2.2 Beam bending

The problem studied in this paragraph is the case of a beam of 192 elements submitted to a force F as shown in the *Figure 3.15*.

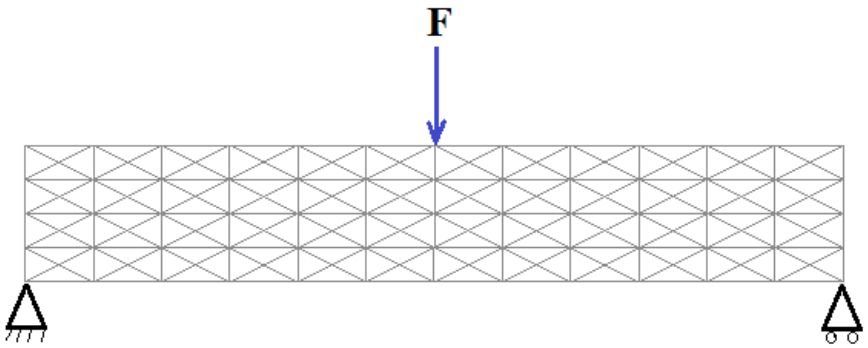

Figure 3.15 : Mesh of the 192-element beam multi-scale example

The final deformation of the beam is presented in the *Figure 3.16*.

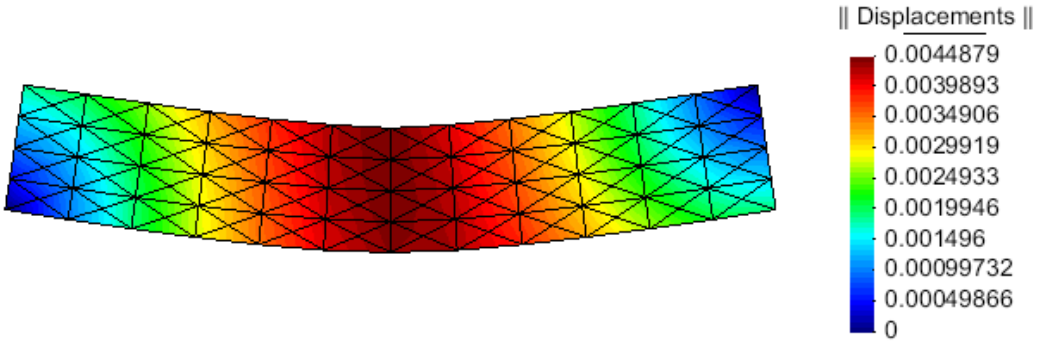

Figure 3.16 : Deformation of the 192-element beam multi-scale example

Similarly to the precedent example various values of the hyper-reduction parameter n_{elem*} are tested. The speed up and accuracy results are presented in the Table 3.8 and the macroscopic load-displacement graphics in the *Figure 3.17* and *Figure 3.18*. The *Figure 3.19* and *Figure 3.20* compare the evolution of the stress versus the load applied for the various values of n_{elem*} .

The no convergence of the case of $n_{\hat{u}} = 4$, $n_{\sigma} = 10$ and $n_{elem*} = 3$ can be explained by the no respect of the relationship (66). Indeed the number of stress components used in here equal to $n_{\sigma*} = n_{elem*}$ x $3 = 9$ which is smaller than the number n_{σ} of stress modes used.

It can be notice that the load-displacement curves are really close to the exact one for whatever values of n_{elem*} . The estimation of the error agrees with that. Indeed the displacement error varies between 3.11% and 5.89% for the hyper-reduction parameters studied. Contrary to the previous example there is no clear increase of the accuracy as the number of elements increases. It seems that using only 5 elements of the 1024-element mesh in the hyper-reduction algorithm to solve the micro-scale problem is enough to obtain accurate results; the error made in this case is only 3.5% in displacement and 2.37% in stress. Moreover a speed up of 84 can be achieved with such hyper-reduction parameters.

$n_{\hat{u}}$	n_{σ}	n_{elem*}	**Speed up**	**Displacement Error**	**Stress Error**
4	10	**3**		**Not converged**	
4	10	**4**	**91.0**	4.10%	7.78%
4	10	**5**	**84.5**	3.50%	2.37%
4	10	**6**	**80.3**	3.39%	1.78%
4	10	**7**	**77.7**	3.11%	3.15%
4	10	**10**	**61.5**	4.52%	2.88%
4	10	**20**	**43.9**	3.48%	1.51%
4	10	**50**	**24.1**	5.89%	2.25%
4	10	**100**	**13.1**	5.28%	0.60%
4	10	**200**	**7.0**	5.22%	0.47%
4	10	**500**	**2.9**	4.86%	0.19%

Table 3.8: Results of the multi-scale problem of the 192-element beam

This second problem composed of 192 elements in the macroscopic mesh enables to point out the efficiency of the whole multi-scale algorithm elaborated during this thesis. Indeed without losing accuracy the computational time of the resolution has been reduced from more than 10 hours using the classical Finite Element model to less than 8 minutes.

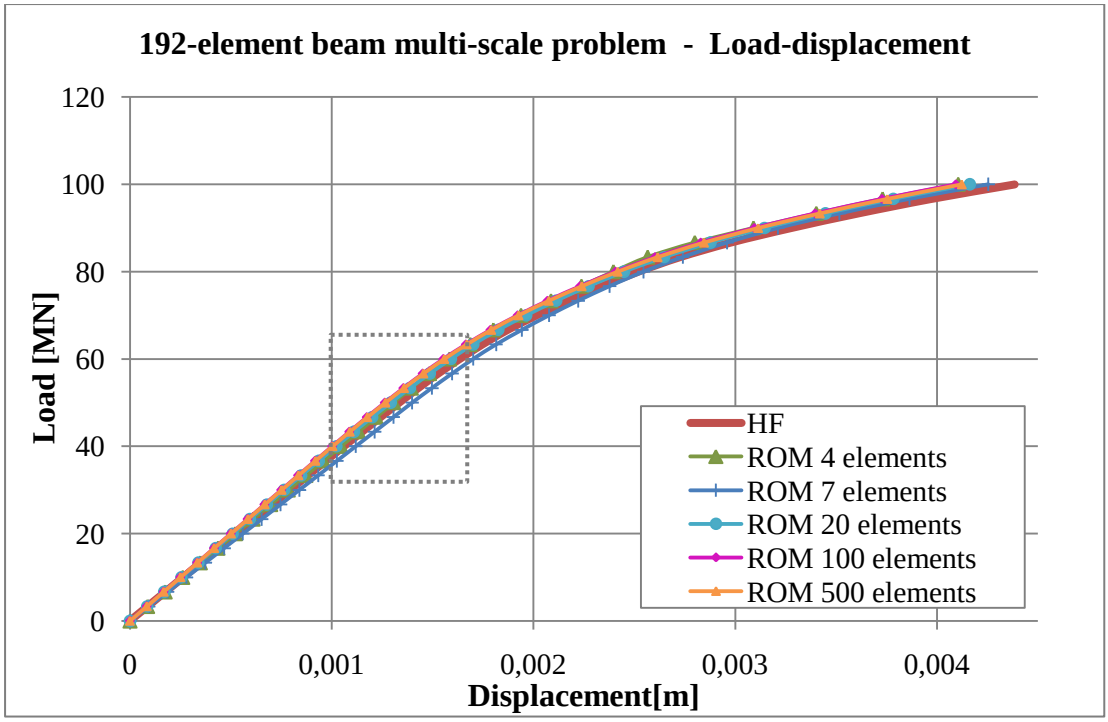

Figure 3.17 : Load-displacement graphics for the resolution of the 192-element beam multi-scale example

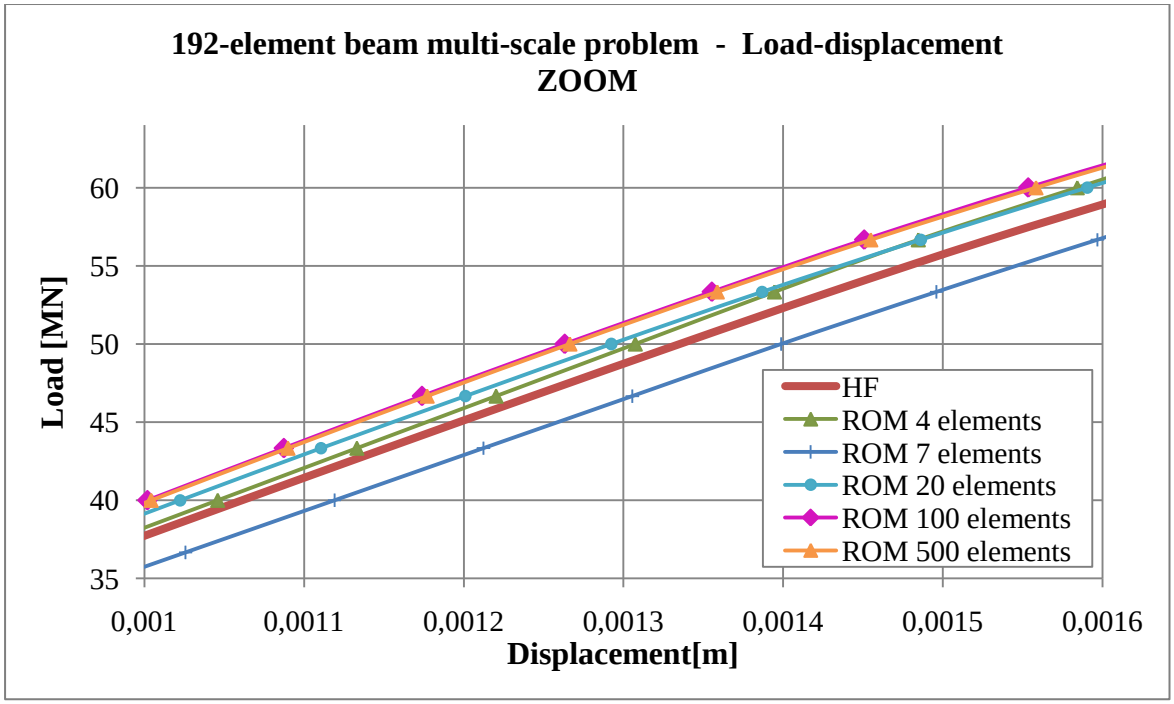

Figure 3.18 : Load-displacement graphics for the resolution of the 192-element beam multi-scale example – Zoom

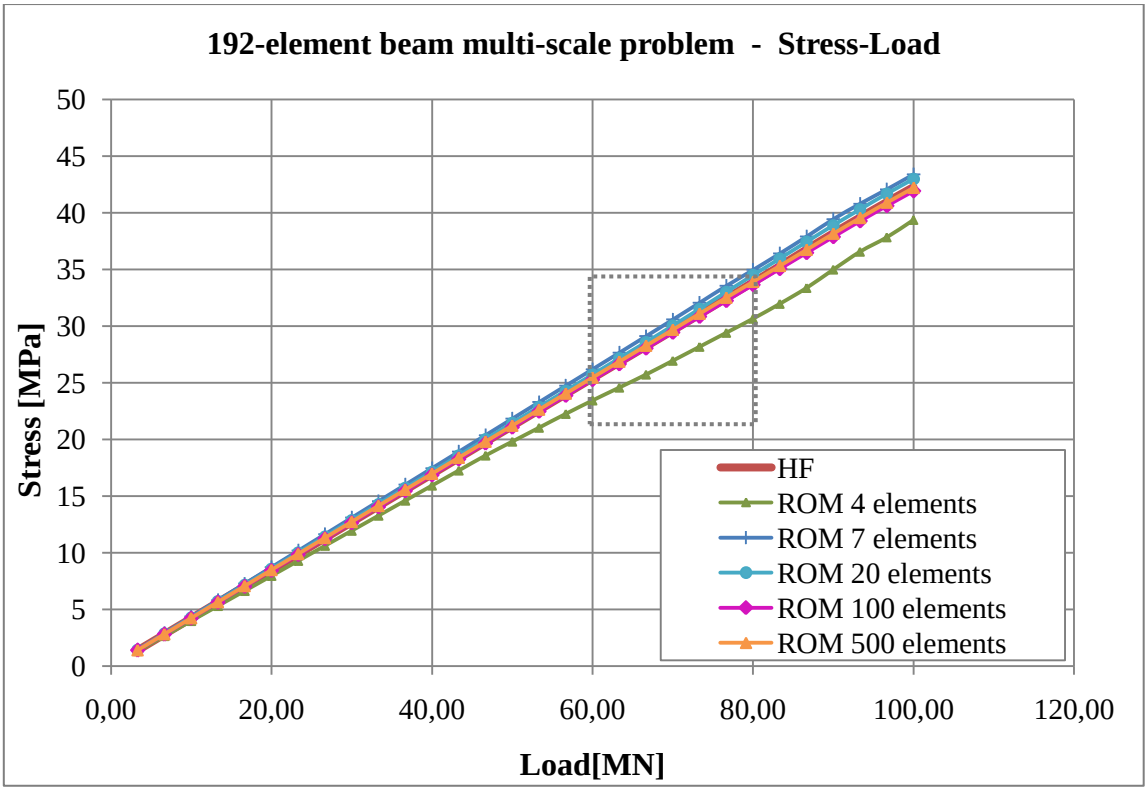

Figure 3.19 : Stress-Load graphics for the resolution of the 192-element beam multi-scale example

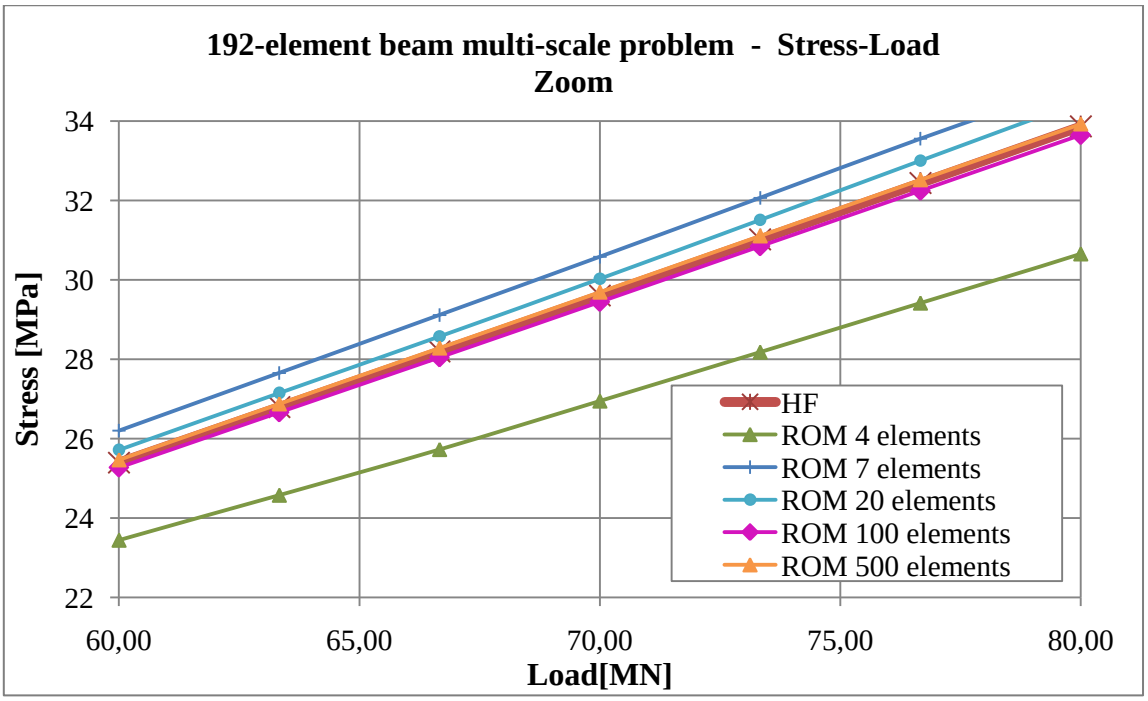

Figure 3.20 : Stress-Load graphics for the resolution of the 192-element beam multi-scale example – Zoom

Conclusion

This Master thesis is dedicated to reduce the computational cost of the multi-scale problems. It proposes to apply model order reduction techniques on the micro-scale problem in the homogenisation process.

The hyper-reduction algorithm developed combines a model order reduction based on a POD-reduced displacement basis with a Gappy Data Reconstruction of the stress tensor. While a single reduction of the displacement space provides a speed up around 1.2 on the resolution of the micro-scale problem the whole hyper-reduction process achieves acceleration around 200 for a 1000-element microscopic mesh and until 400 for a 1600-element mesh without losing accuracy.

Introducing this hyper-reduction of the micro-scale problem in the resolution of a complete multi-scale problem the computational time can be divided by 80 with displacement and stress errors smaller than 10%. The efficiency of this algorithm is mainly due to the Gappy Data Reconstruction technique which enables to reduce the resolution of a 1000-element microscopic mesh to a judiciously selected set of 10 elements.

To go further with this model order reduction method others strategies of stress components selection should be studied to guarantee the stability of the resolution. In order to make it possible to solve macroscopic problems with non-zero boundary

conditions another research field would be to investigate how to apply such conditions to the microstructure.

References

[1] P. Astrid, S. Weiland, K. Willcox, & T. Backx, Missing point estimation in models described by proper orthogonal decomposition, *IEEE Transactions on Automatic Control* , 53-10 (2008), 2237-2251.

[2] K. Carlberg, & C. Farhat, A Compact Proper Orthogonal Decomposition Basis for Optimization-Oriented Reduced-Order Models. *12th AIAA/ISSMO Multidisciplinary Analysis and Optimization Conference* (2008), Victoria, British Columbia, Canada.

[3] K. Carlberg & C. Farhat, A low-cost, goal-oriented 'compact proper orthogonal decomposition' basis for model reduction of static systems, *Department of Aeronautics and Astronautics, Standford University*, California, USA (2010).

[4] K. Carlberg, C. Bou-Mosleh & C. Farhad, Efficient Nonlinear Model Reduction via a Least-Squares Petrov-Galerkin Projection and Compressive Tensor Approximations. *International Journal for Numerical Methods in Engineering* 0 (2009), 1-25.

[5] E.A. De Souza Neto & R.A. Feijóo, On the equivalence between spatial and material volume averaging of stress in large strain multi-scale solid constitutive models. *Mechanics of materials* 40 (2008), 803–811.

[6] E.A. De Souza Neto & R.A. Feijóo, Variational foundations of multi-scale constitutive models of solid: Small and large strain kinematical formulation. *LNCC Research & Development Report* 16 (2006), National Laboratory for Scientific Computing, Brazil.

[7] R. Everson & L. Sirovich, Karhunen-Loeve procedure for Gappy data, *Journal of the Optical Society of America A*, 12-8 (1995), 1657-1664.

[8] M.G.D. Geers, V. Kouznetsova & W.A.M. Brekelmans, Multi-scale computational homogenization: Trends & challenges. *Journal of Computational and Applied Mathematics*, 234-7 (2010), 2175-2182.

[9] Y.C. Liang, H.P. Lee, S.P. Lim, W.Z. Lin, K.H. Lee & C.G. Wu, Proper orthogonal decomposition and its applications - Part I: Theory. *Journal of Sound and Vibration*, 252-3 (2002), 527-544.

[10] D. Ryckelynck, Hyper-reduction of mechanical models involving internal variables *International Journal for Numerical Methods in Engineering*, 77 (2009), 75-89

[11] S. Volkwein, Model reduction using proper orthogonal decomposition. Lecture notes, *Institute of Mathematics and Scientific Computing*, University of Graz (2008).